An observation-driven framework for modeling post-fire hydrologic response: evaluation for two central California case studies

Timothy M. Lahmers[1], Sujay V. Kumar[1], Shahryar K. Ahmad[1,2], Thomas Holmes[1] Augusto Getirana[1,2], Elijah Orland[1,3], Kim Locke[1,2], Nishan Kumar Biswas[1,3], Wanshu Nie[1,2], Justin Pflug[1,4], Kristen Whitney[1,4], Martha Anderson[5], Yun Yang[6]

[1]Hydrological Sciences Lab, NASA Goddard Space Flight Center (NASA-GSFC), Greenbelt, MD, USA.

[2]Science Applications International Corporation, McLean, VA, USA

[3]University of Maryland Baltimore County (UMBC), Baltimore, MD, USA

[4]Earth System Science Interdisciplinary Center (ESSIC), University of Maryland, College Park, MD, USA

[5]USDA-ARS Hydrology and Remote Sensing Laboratory, Beltsville, MD, USA

[6]Cornell University, Ithaca, NY, USA

Corresponding author: Timothy Lahmers (timothy.lahmers@nasa.gov)

Key Points:

- An ensemble soil hydrophobicity parameterization scheme and LAI data assimilation are developed for modeling post-fire hydrological response.
- The assimilation of Leaf Area Index data into the land surface model resolves wildfire-driven evapotranspiration decreases.
- Soil hydrophobicity effects on water balance are less pronounced than LAI, but tend to increase runoff during high flow events.

Abstract

In a warming climate, wildfires are becoming increasingly common, especially in semi-arid environments. Wildfires can disrupt forest ecosystems and induce changes to the land surface. Collectively, these impacts can alter the hydrologic response of a catchment following a fire, resulting in increased potential for surface runoff, reduced evapotranspiration, and, ultimately, a higher risk for flash flooding and mass wasting. The timescale of post-fire recovery of hydrological processes to return to pre-fire conditions is not well established due to the lack of ground measurements. Accurate characterization of the impacts of fire on hydrologic response is also challenging to simulate, given the complex interplay of various processes. Here, we present a generalized framework to quantify the impacts of wildfire on runoff generation. We consider the disturbances in the vegetation and soil as the two main factors contributing to post-fire floods. Using an ensemble modeling structure to account for parameter uncertainty, remotely sensed leaf area index (LAI) is assimilated into a land surface model (LSM) to simulate vegetation disturbance, and the maximum land surface saturation LSM parameter is decreased to parameterize the soil disturbance following observed fires. We consider the impacts of fire-induced changes to LAI and soil saturation on hydrologic states like runoff and evapotranspiration for two case studies. These case studies demonstrate the general applicability of hydrophobicity formulation to serve as a guideline for exploring the range of hydrologic responses post-fire.

Plain Language Summary

Wildfires, which are an important physical process for ecosystems and the land surface, are increasing in frequency in a warming climate. Fires can also cause local changes to the water cycle over affected areas, sometimes leading to an increased likelihood of flooding and soil mass movements. Models are needed to simulate the impacts of wildfire on local hydrology and the chance for flooding. This work presents a methodology that accounts for the impacts of post-fire vegetation and soil disturbances in a gridded model that quantitatively simulates changes to land surface states (e.g., soil moisture) and fluxes (e.g., evaporation and runoff) for a defined land area over time. For vegetation disturbances, we combine remote sensing-based vegetation data with model state variables to account for the effects of fire. For soils, we develop an ensemble-based approach that increases soil runoff following fires through an adjustment to land surface parameters within the model. Using these methods, we analyze the relative roles of vegetation and soil disturbances after fires on runoff and evapotranspiration in two case studies over central California. Our results show the potential for remote sensing data and model parameter adjustment to resolve the effects of fires in the simulation.

Key Words

- Land Surface Modeling
- Data Assimilation
- Fire Hydrology

1 Introduction

In a warming climate, wildfires are becoming increasingly common across the western U.S. (e.g., Reilly et al. 2017; Williams et al. 2019; Higuera et al. 2020, 2021; Hu et al. 2020, Abatzoglou et al. 2021). Globally, fires are shown to increase in some regions under a warming climate (e.g., Flannigan et al. 2012; Moritz et al. 2013, Kumar et al. 2021). In addition to damages to property and populace, changes in the frequency and intensity of fires can also have a wide range of environmental impacts, including disturbing the natural balance of ecosystems, impacting air and water quality, causing increased rates of soil erosion, and increasing the risk of floods and landslides, among others (e.g., Li et al. 2017; Thomas et al. 2021; Wagenbrenner et al. 2021; Hoch et al. 2021). Fires often result in changes to the hydrologic response and water balance more generally, with a shift towards increased streamflow (e.g., Bart et al. 2014). The post-fire recovery of natural environments and associated ecological and hydrological processes may take up to several years and is often affected by the local climate and interannual climate variability (e.g., Wagenbrenner et al. 2021), as well as management practices such as plowing or mulching (e.g., Prats et al. 2016; Viera et al. 2016). From a hydrologic perspective, there are two major physical processes that affect the post-fire response. Disturbances to vegetation and rooting structures can shift hydrological partitioning of precipitation towards runoff processes by decreasing evapotranspiration (ET) (e.g., Li et al. 2017; Kumar et al. 2021). Similarly, fires can alter soil properties, causing reduced infiltration and promoting more surface runoff (e.g., Thomas et al. 2021; Williams et al. 2022). Though both of these processes are reported in the literature, there is significant uncertainty about their precise and interlinked impacts.

Vegetation disturbances due to fire can affect the water balance over affected areas, due to reduced transpiration and indirect impacts on evaporation. Li et al. (2017) showed that global wildfires tend to decrease latent heat (i.e., ET). Ma et al. (2020) considered the impacts of fires on ET in the Sierra Nevada Range and found reduced ET following fires. Reduced ET was proportional to fire severity. This is consistent with the results from Blount et al. (2019), who showed that a fire in the Mill Creek Basin in Montana resulted in a 140% increase in streamflow and a 46% decrease in ET. The same fire also changed the predominant vegetation of the catchment from a coniferous forest to savannah and shrubland. Note that loss of vegetation can affect ET in multiple ways. While loss of vegetation directly reduces pathways for transpiration, thinner canopies also reduce the potential pools for evaporation of intercepted rainwater (e.g., Farres et al. 1987; Fernández-Raga 2017). This reduction of canopy interception can increase runoff and soil erosion from “rainsplash”. The overall impact of fires on ET is a reduction over long periods of time, as shown by recent studies relying on remote sensing measurements in Australia (Kumar et al. 2021) and reduced vegetation productivity after fires in the Brazilian Pantanal (e.g., Kumar et al. 2022). Resolving fire impacts in an LSM can also be subject to uncertainties, as Abolafia-Rosenzweig et al. (2024) found that adjusting Noah-MP LSM vegetation classifications and quantities failed to adequately capture the ET disturbance following two fires in the Pacific Northwest. Furthermore, recovery time periods can vary, as Thomas et al. (2021) showed vegetation recoveries (as a proxy for debris flow generation) of one to two years; however, Ebel (2020) observed a slower ~five-year recovery from remote sensing hillslope observations for a Colorado Front Range Fire. Cuevas-González et al. (2009) also showed, using remote sensing data, that the full recovery of fire-affected forests in Siberia was over 13 years.

The second major impact of wildfires to surface hydrology is the formation of a waxy layer over soils that impedes infiltration, making increased runoff and flooding more likely, often called "hydrophobicity" or "soil water repellency" (DeBano 2000). Hubbert et al. (2012) quantified the impacts of fires on the hydrophobicity of soils in the San Dimas experimental forest and found an increase in repellency to water in grasslands, based on field measurements, but limited changes elsewhere in the catchment following a fire. They also observed elevated discharge and reduced time of concentration during the first year after the same fire, associated with below average precipitation. Soil hydraulic properties can contribute to post-fire hydrophobicity. For example, Ebel et al. (2016) showed that soils with documented post-fire hydrophobicity tended to also have elevated sorptivity relative to pre-fire conditions. They also found that increased runoff persisted for at least three years following fire in a Colorado headwater catchment. Perkins et al. (2022), based on a case study in California, showed that both soil hydraulic conductivity and sorptivity contributed to the potential for increased runoff. Saxe et al. (2018) considered the impacts of fires on streamflow at U.S. Geological Survey (USGS) gages and found moderate burn severity to be associated with increased runoff; however, the impacts of fires on runoff more broadly varied by area and were associated with reduced water yields in some cases.

While the effects of hydrophobicity have been considered throughout the fire-hydrology literature, it remains difficult to estimate or measure the post-fire changes to the soil properties at the watershed scale. The impact of a disturbance on the hydrologic response is also dependent upon the hydrologic connectivity of a basin, as the connection of burned hillslopes to a channel network impacts how quickly increased runoff will reach the channel network (e.g., Hallema et al. 2017). Studies have also used different surface quantities as proxies for hydrophobicity, but they are fraught with considerable uncertainty. Moody et al. (2016) show linear relationships between differences in the delta Normalized Burn Ratio (dNBR) and saturated conductivity and sorptivity of affected soils. However, they also note that this relationship only applies for values of dNBR beyond a threshold of ~420 (smaller dNBR values show too few differences compared to unburned soil). Parameters based on vegetation, such as fire severity from the Monitoring Trends in Burn Severity (MTBS; Eidenshink et al. 2007) dataset, developed by the U.S. Forest Service, have also been demonstrated to be proportional to saturated conductivity and sorptivity (e.g., Ebel et al. 2022). These impacts are consistent with the influence of vegetation on soil properties, where vegetation regrowth results in increased macropore flow and soil roughness to increase soil infiltration (e.g., Ebel et al. 2018). It should be noted that MTBS severity is intended to be proportional to soil exposure; however, differences can arise between MTBS and products based specifically on soil (Eidenshink et al. 2007). Thus, hydrophobicity and vegetation disturbances are closely related, but their specific quantification is difficult.

Similarly, examining the influence of soil hydrophobicity on hydrological processes also involves significant uncertainty. Only a few studies have attempted to model soil hydrophobicity, which rely on case-specific parameterizations or calibrations of the modeling setup. For example, Hoch et al. (2021) calibrated a hydrologic model (with constraints based on observed soil measurements) to estimate the effects of fire on rainfall-intensity-duration thresholds for debris flows. The model was applied in three study areas across the southwest for up to four years following a fire, to monitor recovery. In another study, Thomas et al. (2021) derived a function to use within the HYDRUS 1D model to adjust soil parameters based on Leaf Area Index (LAI) anomalies following a wildfire. From this revised model, they were able to reproduce rainfall-intensity-duration thresholds for debris flows for a case study in the San Gabriel Mountains.

While the methods of Hoch et al. (2021) and Thomas et al. (2021) derived soil parameters following wildfires, they have limitations for general applicability due to the large amount of data required. The former is dependent upon field measurements combined with computationally costly calibration, while the latter does not explicitly examine the impacts of soil and vegetation recovery independently.

Here, we present a framework to represent the hydrologic impact of wildfires using remote sensing data assimilation (DA) and a stochastic representation of the land surface to simulate the change to the surface hydrologic processes following fires. This framework is presented for two case studies, where an increase in USGS streamflow was observed following fires. The key feature of this approach is its ability to resolve both the impacts of both hydrophobicity and vegetation disturbances. The spatially varying nature of hydrophobicity is considered using a flexible stochastic approach. These case studies are intended to demonstrate our approach in a region subject to fires (central California). We note that a broader regional or global study of these impacts with a large number of basins and sample fires is beyond the scope of this work.

Our methodology uses a generalizable remote-sensing DA approach combined with an ensemble of model parameter adjustments within the Noah-MP (Niu et al. 2011) land surface model (LSM) to simultaneously realize the impacts of vegetation disturbances and hydrophobicity. Vegetation disturbances in our model simulations are represented by the assimilation of remote sensing-based LAI, and soil hydrophobicity is parameterized through the adjustment of model parameters based on remote sensing-based fire datasets. The latter is novel because it does not require field measurements or calibration. Instead, the ensemble approach represents uncertainty in the model parameters affected by fires, and their recovery. Given the paucity of reliable reference measurements for water balance terms, particularly around fire events, we here focus primarily on the changes to regional water balance simulated by this generalized approach. Our approach, which does not rely on regionally tuned model parameters and datasets, allows the exploration of the range of hydrological responses post-fire. In that regard, the primary contribution of this manuscript is the conceptual viability of the approach, rather than an application-ready system. The modeled results are also normalized and compared to normalized observed streamflow (see details in section 3), and modeled ET shifts from fires are compared to the Disaggregation of the Atmosphere-Land Exchange Inverse (DisALEXI) dataset (Anderson et al. 2018). We emphasize that the latter is also a modeled product, with biases and errors of its own.

The Noah-MP configuration and parameters used here are consistent with the setup used by the broader community for applications including fire (Abolafia-Rosenzweig et al. 2024), hydrologic modeling (Lin et al. 2018; Lahmers et al. 2022), groundwater modeling (e.g., Barlage et al. 2021), and land-atmosphere interactions (e.g., Dominguez et al. 2020; Barlage et al. 2021). Our technique is demonstrated in two case studies within relatively undisturbed catchments with stream gage data to allow more careful validation; however, the ensemble approach here is intended to be applicable to a broader range of fire circumstances. Using our methods to quantify physical processes affected by wildfires, we consider the following scientific questions for our two case studies:

1) What are the relative roles of vegetation disturbances and hydrophobicity on the water budget changes after a wildfire?

2) What is the range of uncertainty of the impacts of hydrophobicity based on our ensemble approach?

Although these questions are specifically framed to our two case studies in central California, our modeling approach could be adapted and applied to other regions (with additional testing), as wildfire is a global phenomenon.

This paper is organized as follows. In section 2, we describe the modeling and DA configurations. This also includes a discussion of the hydrophobicity parameterization. In section 3, we describe the fire case studies and analysis methods, and results are presented in section 4. Section 4 also includes comparisons of observed ET disturbances and standardized streamflow, compared to modeled impacts. A discussion and summary are included in section 5.

2 Modeling setup and Analysis Methods

2.1 Land Surface Model and Routing Model Configuration

All model integrations are conducted using the NASA Land Information System (LIS; Kumar et al., 2006), which is an open-source framework for terrestrial hydrology modeling and DA. LIS encompasses several state-of-the-art land surface models and DA tools to incorporate a large variety of remote sensing-based land hydrology observations. In this particular study, the Noah-MP LSM (Niu et al. 2011) within LIS is employed at the two selected study areas. For each study domain, three model integrations are conducted: (1) a control or 'open loop' (OL) simulation, where the model is executed using the climatological input of vegetation (LAI) without any DA, (2) a vegetation DA configuration (DA-VEG) where satellite-based LAI retrievals are assimilated to incorporate vegetation disturbances from fires and their impacts, and (3) a model configuration (DA-VEG-SOIL) where impacts of vegetation disturbances and parameterized ensemble soil hydrophobicity are simulated based on remote sensing inputs of LAI and fire characteristics. The initial conditions for all the model integrations are developed by running the model twice from Jan 2001 to Dec 2020 and then reinitializing it in Jan 2001. In the current implementation, we use the TOPMODEL surface and sub-surface runoff scheme and the Simple Groundwater Model (SIMGM; Niu et al. 2007) that represents groundwater storage and water table depth by resolving recharge and discharge processes of the water storage within an unconfined aquifer. Additionally, we employ the prognostic vegetation model of Noah-MP, which includes the Ball-Berry photosynthesis-based stomatal resistance model (Ball et al. 1987) and the dynamic phenology model of Dickinson et al. (1998).

For this study, we used the native Noah-MP parameters developed by the research community. These parameters use information from global datasets and local measurements and have been demonstrated within regional (e.g., Chen et al. 2016; Gao et al. 2017) and global studies (e.g., McNally et al. 2022). These same configurations are also used in other research environments, including for coupling with the atmosphere (e.g., Rasmussen et al. 2023) and for the North American Land Data Assimilation System, phase 2 (NLDAS-2) experiments. Ma et al. (2017) and Cai et al. (2014b) showed that Noah-MP produced reliable results across the CONUS, with improved fluxes compared to other LSMs with NLDAS-2 forcing. Cai et al. (2014a) and Pilotto et al. (2015) also showed reliable Noah-MP results across the Mississippi River basin and the Amazon, respectively. All of these experiments used native parameters. While local calibration may improve the representation of some physical processes and eliminate some regional biases, it also requires reliable, multiple observational constraints on all water budget terms such as precipitation, evaporation, and runoff, making such a task difficult in this domain. Nonetheless, there are numerous studies applying Noah-MP with these native parameters for similar applications in wildfires (e.g., Kumar et al. 2021; 2022) and for other hydrologic applications over the full western US (e.g., Erlingis et al. 2021) that includes the current study area. Here we rely on the native parameters of Noah-MP to preserve the general applicability of the methods.

All model simulations are forced with the boundary conditions from NASA's Modern Era Retrospective Reanalysis (MERRA version 2; Gelaro et al. 2017) dataset. Precipitation is derived from the Integrated Multi-satellitE Retrievals for Global Precipitation Mission (IMERG) dataset (Huffman et al. 2015). The case study domains employed in this study are specified at a spatial resolution of 0.01 degree, with model outputs at 1-day temporal resolution. In addition to the MERRA-2 and IMERG simulations, a set of additional simulations are conducted with atmospheric forcing and precipitation from the NLDAS-2 dataset to evaluate the changes to ET fluxes compared to observations. While not used for further analysis, this simulation is used to examine the consistency of the LSM performance and biases for surface fluxes.

Total runoff (i.e., surface runoff and baseflow combined) derived from Noah-MP is used as input to the Hydrological Modeling and Analysis Platform (HyMAP) routing model to produce spatially distributed streamflow estimates in rivers. Here, total runoff is routed through the river network using the kinematic wave equation. The Courant–Friedrichs–Lewy condition is used to determine HyMAP's optimal sub time steps (Getirana et al., 2017b). One-way coupling of land variables to surface waters is considered (i.e. no influence from floodplains on soil moisture state variables is considered). We opted for one-way, rather than two-way coupling (Getirana et al., 2021) because the basin presents small surface water coverage with little impact on terrestrial water storage (Getirana et al., 2017a). The river network is derived from the Multi-Error-Removed Improved-Terrain (MERIT) Hydro (Yamazaki et al., 2019), and river geometry is derived from empirical equations, following Getirana et al. (2012).

To evaluate the combined impacts of hydrophobicity and vegetation disturbances, changes to water balance quantities across the basin affected by fires are evaluated in the DA-VEG simulation and DA-VEG-SOIL simulation compared to the OL simulation. Differences in ET and runoff components are calculated from derived basin areas for corresponding basins upstream of USGS gages (Getirana et al. 2017b). Analysis of water balance differences allows for the evaluation of the role of surface processes related to fire, irrespective of model biases. HyMAP streamflow is also compared with USGS observations after normalization.

2.2 Vegetation Data Assimilation Setup

To evaluate the impacts of the vegetation disturbance following the wildfires, LAI retrievals from the Moderate Resolution Imaging Spectroradiometer (MODIS) instrument are assimilated into the LSM using a 1-dimensional Ensemble Kalman Filter (EnKF) DA configuration (e.g., Reichle et al. 2002). Specifically, we employ the MCD15A2H (version 6) LAI product available at 500m spatial resolution and at an 8-day interval. Similar to the strategy used in prior studies, daily LAI observations are generated by linearly interpolating between the available 8-day observations (Kumar et al., 2019). This method was also used in Lahmers et al. (2023) for LAI-DA experiments. As noted earlier, in the OL configuration, the vegetation seasonality is prescribed based on the monthly MODIS LAI climatology. This overwrites the dynamic vegetation enabled through Noah-MP.

The EnKF configuration has been widely used in LSM DA studies, including for the assimilation of LAI (e.g., Sabater et al. 2008; Albergel et al. 2018; Kumar et al. 2019 Mocko et al. 2020; Nie et al. 2022), as it enables a convenient way to account for the non-linearities and errors in the LSM physical processes (e.g., Reichle et al. 2002). When a model is executed with EnKF, the states being modified alternate between a forecast (i.e., running the model simulation) and an analysis timestep (i.e., model variables combined with observations), as shown in equation (1). For this equation, let the present forecast timestep be (k) and the earlier analysis timestep be (k-1). The model states are projected forward from ($\hat{\mathbf{x}}_{\mathbf{k-1}}^{+}$) as the model integrates at time k to ($\hat{\mathbf{x}}_{\mathbf{k}}^{-}$). Here, ($\hat{\mathbf{x}}_{\mathbf{k}}^{-}$) are the prior states before DA, which are updated to become the posterior states ($\hat{\mathbf{x}}_{\mathbf{k}}^{+}$). This update occurs when the observations ($\hat{\boldsymbol{y}}_{\boldsymbol{k}}$) and the a priori states ($\hat{\mathbf{x}}_{\mathbf{k}}^{-}$) are combined:

$$\hat{\boldsymbol{x}}_{\boldsymbol{k}}^{+} = \hat{\boldsymbol{x}}_{\boldsymbol{k}}^{-} + \boldsymbol{K}_{\boldsymbol{k}}(\hat{\boldsymbol{y}}_{\boldsymbol{k}} - \boldsymbol{H}_{\boldsymbol{k}}\hat{\boldsymbol{x}}_{\boldsymbol{k}}^{-}) \qquad (1)$$

In equation (1), term ($\boldsymbol{H}_{\boldsymbol{k}}$) is the observation operator, which connects the model and observation states. The Kalman Gain ($\boldsymbol{K}_{\boldsymbol{k}}$) is the weighting factor for forecast innovations ($\hat{\boldsymbol{y}}_{\boldsymbol{k}} - \boldsymbol{H}_{\boldsymbol{k}}\hat{\boldsymbol{x}}_{\boldsymbol{k}}^{-}$), which is computed as a function of the model and observation error covariances, with the model error covariances diagnosed from the model ensemble. In the present study, an ensemble size of 50 is used to ensure sufficient sampling density for diagnosing model error covariances.

To simulate the model uncertainties, small perturbations are added to the model states and a select set of forcing variables as shown in Table 1. These specifications are based on the settings used in prior studies with LAI DA (e.g., Kumar et al. 2021). The forcing state perturbations are enabled every hour, whereas the model state perturbations are employed every 3 hours. Note that perturbation settings for atmospheric forcing also include cross-correlations between variables, to more realistically account for underlying uncertainties. The perturbed forcing variables include longwave and shortwave radiation and precipitation. Note that the forcing and state perturbation and cross correlation settings are established from prior LIS EnKF DA studies (Kumar et al. 2009). The observation error is specified to be a uniform value of 0.05, consistent with previous studies.

2.3 Simulation of Soil Hydrophobicity

Here we develop a generalized observation-informed approach for simulating soil hydrophobicity and the subsequent recovery while acknowledging the underlying uncertainties related to multiple factors including soil and vegetation types, severity of fires, and the type and frequency of precipitation events (Figure 1). The implementation relies on the DA infrastructure within LIS and is informed by multiple remote sensing datasets that characterize fire severity and timing. This configuration leverages an LSM ensemble to realize parameter uncertainty. Note that analysis of the DA-VEG-SOIL simulations compared to other model configurations uses the ensemble mean, except where noted. Specifically, we employ the MTBS (Eidenshink et al. 2007) data, developed by the United States Department of Agriculture Forest Service (USDA-FS) and the US Geological Survey (USGS), and the MCD64A1 (version 6; Giglio 2015) burned area product from the MODIS instruments aboard the Terra and Aqua satellites. The MTBS data maps burn severity using Landsat data and the dNBR algorithm at 30-meter spatial resolution at an annual scale. There are four discrete classes of burn severity defined in the MTBS data: unburned/unchanged, low severity, moderate severity, and high severity. The MTBS data, remapped at 0.01 degree spatial resolution (the same as our model configuration) is used in the soil hydrophobicity parameterization (Figure 2). Note that the highest severity MTBS category indicates combustion of litter and duff layers, and these volatilized layers contribute to hydrophobicity (e.g., DeBano 2000). The MCD64A1 data are available globally at 500m spatial resolution and include information on burn date and quality information.

For resolving fire severity, we acknowledge that other datasets, such as the USDA-FS Burned Area Emergency Response (BAER) data, may be a more direct proxy for soil impacts. The integration of field surveys (Parsons et al. (2010) adds value to this product as a proxy for soil impacts. For example, McGuire et al. (2023) showed that decreases to soil infiltration were not always proportional to burn severity in their observation study of a New Mexico fire. Despite the fact that the MTBS data may be a suboptimal proxy for representing soil impacts, products like BAER data are often not available for every fire. For example, BAER data are only available for one of our case studies. Therefore, a methodology using BAER data would not be practical in many basins. As a result, we chose the MTBS product here because of its wider availability, which makes it more adaptable for any fire, allowing for the scalability of the proposed approach. Yearly MTBS mosaics can be easily and systematically applied to any fire for an LSM simulation. To evaluate this approach, we plotted BAER data on the same grid as the MTBS dataset for one of the focus domains (supporting information; Figure S1). While there is an increase in severity level 3 in BAER, with most of the MTBS points at lower severity, the structural similarity index (Wang et al. 2004) and correlation between the MTBS and BAER product when regridded to the 0.01-degree model grid are 0.52 and 0.76, respectively. These statistics were computed for the full model domain with non-burned areas set to zero. The BAER dataset on the 0.01 degree model grid is also shown in Figure S1. Compared to the MTBS data for this site (Figure 2), much of the BAER dataset is in a higher severity category, despite the spatial patterns of the burn area and severity being consistent with the MTBS dataset.

The soil hydrophobicity implementation is designed to simulate the repellency introduced into the soil after intense heating. The repellency leads to a reduction in infiltration into the soil, impacting the partitioning of water at the soil surface, as discussed in section 1 (e.g., Ebel et al. 2018; 2020; 2022; Thomas et al. 2021; Wagenbrenner et al. 2021). Figure 1 provides a schematic of the soil hydrophobicity implementation developed within the LIS framework. The locations with soil hydrophobicity are identified based on the landcover type and the severity of fire, based on the MTBS dataset. First, soil repellency is not simulated over locations with bare soil (i.e., without a true vegetation type), as the burning of the litter and organic material is the primary reason for the development of a waxy layer on the soil. Second, based on the severity of the fire (low to high severity as defined by the MTBS data), different levels of soil hydrophobicity and recovery are simulated, with areas of higher severity being assigned a range of soil disturbance perturbations that are greater. Each MTBS category (unburned/unchanged, low severity, moderate severity, and high severity) is assigned its own range of possible disturbance perturbations. The infiltration process within Noah-MP (in the SIMGM model) is primarily controlled by the maximum surface saturation fraction parameter (*FSATMX*), which is defined as a global constant in the LSM. Once fire occurrence is determined at a grid point (based on MTBS and MCD64A1), the *FSATMX* value is increased to simulate the increased soil repellency at that location. Note that this parametrization will not have any effect in frozen soils, as saturated area goes to zero in conditions with frozen soil (see equation 2 of Niu et al. 2007). On subsequent days following the fire instance, an exponential recovery of *FSATMX* back to the original value is simulated based on the following equation:

$$\mathrm{FSATMX}'_{\mathrm{k}} = \max\left(\mathrm{FSATMX}, \frac{\mathrm{FSATMX}}{\left(1-e^{\frac{-\delta t}{K_k}}\right)}\right) \qquad (2)$$

where $FSATMX$ and $FSATMX'_k$ represent the original and updated values of the maximum surface saturation fraction parameter, δt is the time elapsed since the fire, and K_k is the recovery constant value. The subscript k represents the ensemble member (50 members in total). For each ensemble member, a different time scale of recovery is simulated by sampling K_k from a Gaussian normal model distribution, based on MTBS burn severity categories. A different range of the scale of recovery is used for each MTBS category, with three possible values shown in Figure 2c. These categories are regridded to the model resolution for each basin. For high severity locations, the K values are sampled from a range that simulates a three-year recovery. Similarly, for moderate and low severity locations, the sampling of K values is chosen to simulate a two- and one-year recovery, respectively. These different timescales for different fire severity are enabled by the fire recovery factor, ω (Figure 1c) that determines how quickly FSATMX returns to normal. Note that this process is not otherwise included in the Noah-MP source code, as FSATMX is a global constant. This modeling assumption is consistent with the results of Thomas et al. (2021), who showed soil recovery within one to two years of a fire through modeling and Perkins et al. (2022), who had similar findings from observations. However, soil recovery could potentially be longer (e.g., Ebel 2020).

Additionally, our soil hydrophobicity formulation includes parameterization to speed up the recovery if substantial rain events occur post fire. This dependency is based on two assumptions. First, we assume that post-fire runoff and erosion will remove some of the hydrophobic soils (e.g., Moody et al. 2013; Hoch et al. 2021), and we attempt to parameterize that here. Secondly, this assumption is consistent with the faster ecosystem recovery of fires with increased precipitation (e.g., Anderegg et al. 2015), where re-established vegetation can break down hydrophobic soils, such as through the re-establishment of rooting systems (e.g., Robichaud et al. 2016). The precipitation adjustment is performed by comparing the daily accumulated precipitation to the monthly rainfall climatology. If the daily accumulated precipitation is four times larger than the monthly average rainfall, then the recovery factor (K_k) is decreased. The factor of four was chosen with the idea of screening for rainfall events that are large enough to reduce the hydrophobic behavior of the soil. We acknowledge that the choice of this factor can be improved with localized soil measurements around fires. Finally, if a new fire event occurs at the same location, the increase in *FSATMX* and the subsequent recovery shown in Figure 1b are repeated.

The level of decrease of FSATMX back to equilibrium is also determined based on random sampling. Unlike prior studies, our parameterization is not deterministic and acknowledges the associated uncertainties that are likely present in a soil hydrophobic environment post-fire.

2.4 Analysis of LSM Fluxes

For these case studies, we evaluate the behavior of our model compared to prior fire-hydrology literature (as outlined in the previous section) and with observations of USGS streamflow and ET anomalies. A direct evaluation of the changes in modeled fields with observations around the fire events is difficult, given the paucity of reliable ground observations. We are able to compare the model results to ET from the Disaggregation of the Atmosphere-Land Exchange Inverse (DisALEXI) dataset (Anderson et al. 2018). DisALEXI is also a modeled product informed by remote sensing observations of land surface temperature and is subject to biases of its own. The DisALEXI dataset is distributed through OpenET (Melton et al., 2021) and is currently available from January 2016, slightly more than a half year before the fire. We therefore compare the ET trends of the first six months of 2016 (pre-fire) with the same months of 2017 (post-fire). Note that this period is also a transition from a relatively dry to a relatively wet period. Due to the incomplete nature of debris flow records and field measurements throughout the western US following fires, additional validation is not possible; however, we also perform this validation using the alternative LSM simulation with NLDAS-2 forcings.

To assess how the simulations with LAI DA resolve the impacts of the vegetation losses following fires, we evaluate the basin average LAI for all three simulations and changes to ET in the DA-VEG and DA-VEG-SOIL simulations, compared to the OL simulation. This analysis is for three years following the fires, to analyze the recovery compared to other fire literature (e.g., Wagenbrenner et al. 2021).

We also evaluate all Noah-MP water balance fluxes and the change in terrestrial water storage (TWS) as a percentage of precipitation for the year following the wildfire. This enables us to understand the impacts of incorporating vegetation disturbances and parameterized hydrophobicity for soil disturbances on specific water balance terms. ET and total runoff percentages are considered, along with their individual components (i.e., transpiration, canopy evaporation, and soil evaporation for ET and surface and sub-surface components for runoff) for three years after the fires.

Finally, we evaluate the timeseries of LSM flux changes for the first year after the fires. The impacts of fire (through the vegetation and soil disturbance) are also evaluated as percent changes of ET (including all of its Noah-MP components) and runoff (including its surface and sub-surface components) compared to the OL simulations for all three years after the fire. The differences between model timeseries are tested for statistical significance using the non-parametric Wilcoxon Rank Sum test (Gibbons et al. 2011), available in MATLAB (Wilcoxon signed rank test 2024). This test is sensitive to cases where paired values (e.g., DA-VEG vs. OL and DA-VEG-SOIL vs OL) in one series are consistently greater than the other, as is true in our case studies, even when the differences are small.

3 Observed Fire Impacts

In the present study, we selected two fire cases. The paucity of USGS reference gages (i.e., sites with no upstream diversions and limited human interference) with fires that occurred upstream during recent data records limits our ability to do a broader analysis with more gages. The first case is associated with a significant observed hydrologic response following the fire, due to a larger percentage of the basin that was burned. The second case is also associated with high streamflow following the burn; however, the burn area relative to the size of the basin was considerably smaller. Above average streamflow is observed during the first year following both fires, as we show with standardized indices in more detail. Both fires occurred near the coast in central California (Figure 2). Note that these specific cases may not be representative of global fires or of other regions of the western US.

3.1 Big Sur Case Study

The first case is a fire that affected the Big Sur State Park along the coast of central California (Figure 2). This fire (the Soberanes Fire) ignited on 22 July 2016 and burned nearly all the drainage area upstream of USGS gage 11143000 (Figure 3a). Note that this gage is a USGS Gages-II reference basin, meaning it has limited human modifications and no diversions. USGS streamflow (available online at: https://waterdata.usgs.gov/nwis/rt) at this gage was substantially higher in WY2017 (Figure 3b) following the fire event.

The anomalous nature of the streamflow during this year is reflected by the Standardized Streamflow Index (SSFI) (computed based on 18 years of data from WY2003 through WY2020). A procedure similar to the calculation of standardized precipitation index (SPI; McKee et al. 1993) is used to derive SSFI. Here SSFI is derived by fitting the record of observed flow to a skewed distribution (3-parameter log-normal). This distribution has been used for streamflow fitting in different regions (e.g., Tijdeman et al. 2020) and demonstrated to produce robust results for SSFI. From the new distribution, daily streamflow is converted to a percentile, which is then used to derive a z-score on a normal distribution. The result is a streamflow timeseries with gaussian characteristics. Note that observed streamflow cannot be lower than zero, so a derived (negative) z-score for zero streamflow based on the normalized distribution is the minimum value of SSFI. From this analysis, SSFI values in excess of 3.0 are observed during the WY2017 cold season (Figure 3c). This indicates anomalous streamflow that is 3.0 standard deviations from normal during the year following the fire. Furthermore, the annual flow duration curve (FDC; top 20th percentile is shown) for WY2017 exceeds the 95th percentile of annual FDCs from WY2001 through WY2022 (excluding the three years following the fire) (Figure 3d). WY2019, three years after the fire, is also much above average. The 95th percentiles were computed by fitting each probability of exceedance of the curve onto a normal distribution. Thus, this is a case where significant increases in streamflow happened in the year following a wildfire. WY2017 was a wetter than average year for much of California (CNRFC 2017), so while we cannot argue that the fire alone was responsible for this hydrologic response, the anomalous nature of the peak flow suggests it likely contributed to the observed increases to streamflow. Similarly, 30-day SPI (based on basin average IMERG precipitation) was above normal for WY2017 but remained close to ~1.5 standard deviations throughout the 2016-2017 winter. This suggests that while precipitation was above average, it was not as anomalous as the post-fire observed streamflow.

3.2 Bryson Case Study

The second fire case affected a catchment near Bryson, CA, which is also dominated by cold season runoff. This is evident from the annual cycle of streamflow, where most of the runoff in the basins of interest (Figures 3-4) occurs near the beginning of each year (i.e., mid-winter into early spring). In this case, the fire (the Chimney Fire) ignited on August 13, 2016 and burned some areas of the lower basin above USGS Gage 11148900 (Figure 4a). This gage is also a USGS gages-II reference basin. Note that this fire, while containing more severe impacts, burned a smaller percentage of the basin compared to the Big Sur case study. The impacts of this case are also complicated by some less severe fires upstream in the basin, from summer 2015 and earlier in 2016. These additional mild burn areas to the north of the gage are shown in Figure 4a and are accounted for in the model simulations with LAI DA (DA-VEG) and the hydrophobicity scheme (DA-VEG-SOIL). The Chimney fire has a more significant impact on localized LSM fluxes due to its greater severity, as will be shown later. Following the more severe 2016 fire, WY2017 was associated with above average peak streamflow, despite the rest of the year being average or below average. This above average streamflow is reflected in the SSFI (Figure 4c), with anomalies of over ~2.5 standard deviations for WY2017. Above average SPI with slightly more than 1.5 standard deviations was also observed in early 2017. We again note that SSFI and SPI normalized values cannot be lower than the normalized value equivalent to zero, and this affects the range of SSFI and SPI values in Figure 4c. From the top 20% of the FDC, much of this year exceeded the 95th percentile. Elevated flow also occurs in WY2019. The causes of the high flow following this fire are more complex than in the first case study, due to the combination of the mild fires in the upper basin from the preceding year and the limited area affected by the more severe fires. The limited area of the fires could also make the subsequent hydrologic response more sensitive to hydrologic connectivity of the basin (e.g., Hallema et al. 2017). Furthermore, while this basin experienced above average streamflow compared to other years, the streamflow anomalies are not as extreme as in the Big Sur case.

4 Results

4.1 Modeled and Remotely Sensed ET and Streamflow Disturbances

We compare the LAI and ET changes from the DA integrations (i.e., DA-VEG) to the OL simulation in Figure 5. Note that this figure includes the timeseries of basin averages. Figure 5 shows that estimates of LAI and ET from the DA-VEG and DA-VEG-SOIL are similar to OL prior to the fire event, whereas they diverge from the OL simulation, with reduced LAI in the DA-VEG and DA-VEG-SOIL simulations, following the fire upstream of USGS gage 11143000 (i.e., the Big Sur case). It takes three years for the LAI in the DA-VEG and DA-VEG-SOIL simulations to approach the OL simulation, which is based on prescribed LAI climatology (Figure 5). LAI approaching climatology would be a proxy consistent with recovery. This is consistent with the literature on vegetation recovery, showing similar timescales of post-fire recovery (e.g., Thomas et al. 2021); however, other studies have shown longer recovery (e.g., Ebel 2020). Noah-MP LSM ET anomalies follow a similar pattern, where both simulations that include LAI-DA are nearly the same and approach the control simulation after approximately three years.

The vegetation disturbance and recovery for the USGS 11148900 basin area (i.e., the Bryson case) are less pronounced, as a large area upstream of this gage was either not burned or burned from an earlier fire during summer 2015. Basin averaged LAI in the DA-VEG and the DA-VEG-SOIL simulations is less than the OL simulation, even before the 2016 fires. This likely also reflects drought conditions that affected the basin. LAI differences begin lower for the DA-VEG case prior to the fire and stay lower beyond the fire (Figure 5c). By the third year following the Bryson Fire, LAI again approaches climatology, consistent with the Big Sur case. ET anomalies are somewhat less pronounced for this basin and vary with seasonality; however, the pattern of disturbance following the 2016 fire followed by a slow recovery during the following years is consistent with the prior case study and literature (e.g., Thomas et al. 2021).

The LSM was also run with NLDAS-2 forcing for both sites (only for LSM ET validation), to demonstrate the consistency of the model results irrespective of forcing (Figure S2). For these runs, NLDAS-2 forcing results in similar patterns to simulations forced with MERRA-2 atmospheric forcing and IMERG precipitation, with reduced LAI from fires and ET anomalies that recover after 3-years. This demonstrates consistency with the model processes, regardless of the forcing used.

Modeled post-fire ET trends (January through June 2017 vs 2016) are compared to the DisALEXI product, used as the reference. As seen in Figure 6, the realization of the ET trends around the fire are different between DisALEXI and the LSM estimates. For example, the DisALEXI data show a significant reduction in ET during the post-fire period compared to the pre-fire period (Figure 6a,e) over the basin areas corresponding with the fires (see Figure 2b and Figure 2c as a comparison) for both USGS gages 11143000 and 11148900. However, the OL simulation (Figure 6b,f) shows ET increases across both basins, reflecting a wetter 2017 than 2016 without any evidence of wild fire impacts. The DA-VEG simulations (Figure 6c,g) and DA-VEG-SOIL simulations (Figure 6d,h) also show increases to ET across the study areas due to the generally wetter conditions in 2017 than 2016. However, the increases to ET are smaller over the burn areas and closer to zero (in both the DA-VEG and DA-VEG-SOIL simulations). While these are more neutral compared to the OL simulation, the reduced magnitude of ET changes prevents the LSM from capturing the spatial patterns of the ET over time, in contrast to the DisALEXI dataset. The same spatial patterns occur in LSM results that were forced with NLDAS-2 precipitation (Figure S3).

There are several reasons for the apparent mismatch in the pre- and post-fire responses in ET simulated by DisALEXI and our model simulations. DisALEXI is an energy balance model that uses time-differential satellite land surface temperature observations as the primary input with little reliance on the moisture (precipitation) inputs. On the other hand, the LSM (Noah-MP) includes both energy and water balance considerations. The finer resolution of DisALEXI allows more detailed characterization of fire impacts, which is limited in the LSM simulations. To investigate the differences in the ET patterns from these models further, we examined the responses of the components of ET. As shown in Figure 7, the transpiration component of ET has a small increase in the OL simulations but a decrease following the disturbance for the DA-VEG and DA-VEG-SOIL simulations. Note that the spatial patterns of changes in transpiration from fires are similar to those of the ET changes in DisALEXI. However, within the LSM, the decreases in transpiration are compensated by the increased soil evaporation (discussed in the next section), and as a result, the total ET from the LSM does not show a reduction in total ET similar to that of DisALEXI. In other words, the vegetation disturbance realized through LAI DA does capture the impacts of fires on ET, but to a lesser extent compared to DisALEXI. However, differences in the underlying model formulations and the resulting biases in the magnitudes of ET make it difficult to conduct a consistent evaluation of the model simulations.

To develop comparisons of streamflow, we extended the modeling setup to include the HyMAP streamflow routing model (see details in Section 2.1). Modeled SSFI is compared to the observed

SSFI (both quantities are derived with data from WY2003 through WY2020; Figure 8).

We perform the comparisons of streamflow in the normalized SSFI space, acknowledging the biases in the modeled streamflow estimates. Results show that the DA-VEG and DA-VEG-SOIL simulations produce higher SSFI values in the years following the fire (especially year-one). Note that for USGS gage 11148900, the DA-VEG and DA-VEG-SOIL peak flow for WY2017 is higher than SSFI from observations. The DA-VEG and DA-VEG-SOIL simulated SSFI is generally higher than the OL SSFI for periods of peak flow, even into year-two and year-three following the fire. These higher values tend to be closer to the observed SSFI during the later years, showing the added value LAI DA and parameterized hydrophobicity for modeled streamflow. It should be noted that differences in SSFI may not be one-to-one with changes in the quantity of streamflow due to SSFI being a scaled variable (i.e., proportional to a z-score). The magnitude of changes to SSFI, where smaller relative changes for higher values of streamflow occur in earlier years, are thus not directly proportional to changes in the actual water balance. The latter quantity is explored further in the next section.

4.2 Simulated Changes to Water Balance

Water balance changes for year-one are shown in Tables 2-3 and in Figures 9-10. For the Big Sur case (Table 2), total ET in the year following the fire drops from 60.6% in the OL simulation to 55.1% and 54.5%, in the DA-VEG and the DA-VEG-SOIL simulations, respectively. Most of this change is caused by transpiration, which drops from 24.7% in the OL simulation to 16.9% and 16.8%, in the DA-VEG and the DA-VEG-SOIL simulations, respectively. The canopy evaporation term is associated with smaller decreases, while soil evaporation increases. Total runoff increases from 28.4% in the OL simulation to 31.9% in the DA-VEG simulation. The hydrophobicity parameterization further increases total runoff to 32.6%. For the DA-VEG simulation, sub-surface runoff increases to 26.2% (from 23.4% in the OL simulation), while the impact to surface runoff is small (5.0% in the OL simulation to 5.7% in the DA-VEG simulation). Hydrophobicity decreases sub-surface runoff, while increasing surface runoff, a potential source for flash flooding, to 7.3%. Changes to soil moisture and groundwater (i.e., total TWS change) have a net increase, where loss of vegetation results in additional TWS storage during the year after the fire, in both the DA-VEG and DA-VEG-SOIL simulations.

Annual accumulated ET and total runoff for the three years following the fire (resetting on the date of ignition) are shown in Figure 9, and the impacts of both the vegetation disturbance and the soil disturbance are more clearly reflected here. For ET, the DA-VEG simulation closely follows the DA-VEG-SOIL simulation, showing that the vegetation disturbance significantly reduces ET. The three-year average spatial impacts (shown as percentages that are normalized by annual precipitation) are shown in the lower panels of Figure 9, and they demonstrate that the LAI-DA decreases ET by nearly 10% in some places for the DA-VEG vs OL simulations (Figure 9). Increases in runoff are of a similar order of magnitude (Figure 9). The relative impacts of the soil disturbance are smaller (Figure 9c, f) but still present. As runoff is a smaller term (note the differences in the y-axes in Figure 9d), the relative impacts of the soil disturbance on runoff are more easily visible in the accumulated runoff timeseries. Total runoff diverges from the OL simulation more quickly in the DA-VEG-SOIL solution compared to the DA-VEG simulation. Thus hydrophobicity played a more critical role during the winter following the fire, despite its smaller net impact. In the accumulated runoff and ET plots, some differences persist through year-three. There are also a few localized areas where the soil disturbance has a greater impact (Figure 9c, f).

Changes to the water balance are less pronounced for the Bryson case, given the relatively smaller burn area upstream of USGS gage 11148900 (Table 3) and potentially smaller degree of connectivity (e.g., Hallema et al. 2017). The percentage of total ET for year-one drops from 59.7% in the OL simulation to 58.7% in the DA-VEG simulation. The change from hydrophobicity is marginal, as the total ET is 58.6% in the DA-VEG-SOIL simulation. These changes are primarily from reduced transpiration, which drops from 23.4% (OL) to 21.6% in the DA-VEG simulation. The increases to soil evaporation also occur in this case. Total runoff increases from 27.2% in the OL simulation to 29.7% in the DA-VEG simulation and 29.9% in the DA-VEG-SOIL simulation. Here, the net impacts of hydrophobicity are nominal. For this case, total changes to TWS are in the opposite direction, dropping from 13.2% (OL) to 11.7% (DA-VEG).

The net changes to ET and total runoff for the three years following the fire are shown in Figure 10. As shown from the water balance changes in Table 3, ET decreases in the DA-VEG and DA-VEG-SOIL simulations (Figure 10a). The DA-VEG and DA-VEG-SOIL results are extremely similar, as hydrophobicity has little impact on this gage. For total runoff, the effects are similar (Figure 10d), as the DA-VEG and DA-VEG-SOIL simulations result in increased runoff; however, runoff in the DA-VEG-SOIL simulation still diverges slightly from the other two simulations in year-three. Thus, the impacts of hydrophobicity should not be entirely ruled out, even much later. These results (averaged over three years) are also plotted spatially for the full basin, and they show smaller ET and runoff changes compared to the Big Sur case, except for the southeast corner of the basin that was affected by the severe burns (based on the MTBS data; Figure 4). Despite the impact of hydrophobicity being small over much of the basin, there are more pronounced ET and runoff shifts over the burn areas in the DA-VEG-SOIL plots compared to the DA-VEG plots.

4.3 Progression of Hydrologic Processes

Percent changes in basin average fluxes compared to the OL simulation and their statistical significance are shown in Table 4. This includes all three years of analysis. All our results are statistically significant based on the Wilcoxon Rank Sum test, even in cases where the absolute value of the average differences is relatively small. We plot the timeseries of anomalies for the specific components of ET and Runoff in Figures 11 -12 to show the temporal variability of different components. This timeseries is only plotted for the first year following the fire, when the impacts are the greatest.

For the Big Sur State Park case, the vegetation disturbance from fire decreases the total ET (Table 4), consistent with the water balance changes shown in the previous section. This is primarily driven by the decreases to transpiration (Table 4; Figure 11a) during the first year after the fire. The impacts of the fire on transpiration and ET are reduced during the drier year-two and continue to be lower through year-three (Table 4). Nearly all of these changes are driven by LAI-DA (as realized in the DA-VEG simulation). There is also an increase in soil evaporation as vegetation is removed (Table 4; Figure 11b) and a slight decrease to canopy evaporation (due to the loss of intercepted rainfall; Table 4; Figure 11c). The reduction in ET for each year following the fire is also shown in Figure 9. As discussed in the previous section, the increase to soil evaporation associated with the vegetation loss is expected; however, Noah-MP is likely overestimating it, given the more pronounced impacts of fire on ET in prior literature (e.g., Thomas et al. 2021). It is likely the cause behind the reduced magnitude of the ET disturbance compared to observations (Figure 6). The increases to bare soil evaporation shown in Noah-MP likely also decrease post-fire runoff to some extent. Bare soil evaporation anomalies diminish by year-two and year-three, following the fire (Table 4). The soil disturbance parameterization reduces infiltration, which has the effect of reducing soil evaporation in the DA-VEG-SOIL simulations, compared to the DA-VEG simulation (Figure 11b; Table 4).

Modeling vegetation and soil disturbances shows that both impact the runoff estimates for the Big Sur fire. The reduced transpiration increases both the surface and sub-surface components of runoff in the DA-VEG case (Table 4; Figure 11d,e). When the soil disturbance is included (i.e., DA-VEG-SOIL), there is a significant shift in the hydrological partitioning with a more substantial increase in surface flow (Figure 11e). Further, as infiltration into the soil becomes more restricted, the soil hydrophobicity formulation also results in comparatively less sub-surface flow (Figure 11d). These results demonstrate a fairly high spread in surface runoff between ensemble members for the DA-VEG-SOIL simulation, which represents the uncertainty of the hydrologic response from multiple factors associated with the soil recovery. The range of ensemble simulations for the DA-VEG-SOIL configuration is shown in Table S1 of supporting information, and it demonstrates that surface runoff changes in the DA-VEG-SOIL simulations range between 36% and 57% in year-one, and correspond with net runoff increases between 12% and 18%. The higher end of this spectrum demonstrates that the hydrophobicity in the model can cause flooding, consistent with the observed streamflow anomalies. The impacts of ensemble spread are less for other model variables and diminish for the runoff terms in year-two, but rebound slightly during the wetter year-three. Despite the smaller impact on the overall water balance, this component of the soil disturbance should not be overlooked due its potential to enhance flash flooding. While the effects of the vegetation disturbance are more persistent, the impacts of hydrophobicity on surface runoff are lessened by the second half of year-one (Figure 11e), and they diminish substantially by year-two and year-three (Table 4). Model soil moisture is also impacted in the DA-VEG and DA-VEG-SOIL simulations (Figure 11f). In the DA-VEG simulation, 0-10 cm soil moisture increases during the cold season of year-one, compared to the OL simulation. During the rest of year-one, loss of vegetation reduces soil moisture, and these reductions are greater in the DA-VEG-SOIL simulation, where infiltration into the soil column is further reduced.

For the Bryson, CA case, the impacts of the vegetation disturbance (realized in the DA-VEG case) are similar to Big Sur case, but less due to the relatively smaller burn area. The total ET in years one through three is also reduced for this case, but to a lesser extent (Table 4). The vegetation disturbance reduces the transpiration component of ET, regardless of soil hydrophobicity, as depicted in the timeseries of anomalies for year-one (Figure 12a). As in the previous case, these transpiration anomalies are more substantial in year-one following the fire compared to years two and three (Table 4). Canopy evaporation is also slightly reduced for this case (Table 4; Figure 12c). Bare soil evaporation also increases in response to the vegetation disturbance in both the DA-VEG and DA-VEG-SOIL simulations (Table 4; Figure 12b), even though total ET remains negative due to the fire (Table 4). Compared to the Big Sur case, the magnitude of all these components is smaller, likely due to only a fraction of the basin area being affected by the wildfires (Figure 4).

For runoff, the effects of vegetation losses, realized in the DA-VEG simulation also occur in the Bryson, CA case. Sub-surface runoff in both simulations increases (Table 4; Figure 12d). The effects of soil hydrophobicity are relatively small in terms of the water balance for surface runoff (Table 4; Figure 12e); however, the ensemble spread depicted in supporting information (Table S1) shows percent increases as high as 15% in year-one and 12% in year-three. This indicates a slower recovery with more potential for flooding despite the smaller impact of the soil disturbance. The smaller but potentially variable impact of the soil disturbance from hydrophobicity could also reflect the impacts of hydrologic connectivity (e.g., Hallema et al. 2017) in the basin. In this case, the hydrophobicity parameterization does not have a compensating effect on sub-surface runoff (Figure 12d). Surface runoff increases in the DA-VEG simulation (Table 4; Figure 12e), which is expected given the high observed streamflow during the 2016-2017 winter (Figure 4). The increases in surface runoff in the DA-VEG, and to a lesser extent from DA-VEG-SOIL, simulations in the timeseries in Figure 12 also appear in the fluxes and water balance, shown in the previous section (Figure 10). The ensemble spread shown in the runoff components (Figure 12d,e and supporting information Table S1) implies there are some ensembles where the impacts of hydrophobicity are greater. Thus, the ensemble spread shows that some solutions could have greater surface runoff, which would be more consistent with the higher observed USGS flow for WY2017 (Figure 4). 0-10 cm soil moisture in year-one of the DA-VEG simulation and the DA-VEG-SOIL simulation slightly decreases or has very little difference compared to the OL simulation for most of the year, except during the cold season when it increases.

5 Discussion and Summary

In this study, we present a generalized approach to characterize the effects of wildfires on vegetation and soils to account for changes in hydrological partitioning. This is examined using two case studies. In the first case, in Big Sur State Park, where nearly the full basin is burned, changes to vegetation reduce transpiration over the three years following the fire. The greatest impacts are during the first year, and losses to transpiration and increases in bare soil evaporation, sub-surface runoff, and surface flow are observed. The effects of soil hydrophobicity are smaller. However, these impacts, combined with the effects of vegetation, increase surface runoff and the potential for flooding. The soil disturbance has the greatest impact during more significant runoff events. Thus, our model simulations capture increased surface flow, coinciding with much above average observed streamflow.

This study follows a robust LAI DA approach based on earlier work, where LAI DA was shown to significantly alter the water balance following the Australia wildfires (Kumar et al. 2021). Here, we build on the methodology of Kumar et al. (2021) by adding modeling components to simulate fire induced soil hydrophobicity, which is unprecedented in the literature. The results of our analysis, in the context of these specific cases, are consistent with the findings of Kumar et al. (2021) and with prior fire literature showing the impacts of the disturbance on the water balance. Note that ground records and measurements of fire impacts, such as debris flows, in the

Big Sur and Bryson study areas are limited. Consequently, a thorough evaluation of the model simulations from this study against ground reference data is impossible.

The LSM in the present study uses the native parameters developed for global studies. No regional calibration of the model was performed in this study to maintain the generic nature of the model formulations. Therefore, direct comparisons to streamflow are not included. However, both vegetation and soil disturbances increase the modeled SSFI in a way that is consistent with observations. Additionally, the reductions in ET caused by fires are consistent with independent satellite-based estimates (i.e., DisALEXI); however, the sign change in the LSM simulations (with and without fire impacts) remains incorrect in the 2016 to 2017 trends due to model biases. The tendency of the model to increase bare soil evaporation caused the impacts of LAI DA to be substantially reduced, compared to ET patterns realized in the DisALEXI dataset. This is consistent with Abolafia-Rosenzweig et al. (2024), who also found that enhanced post-fire bare soil evaporation in Noah-MP had a compensating effect on transpiration losses, to limit the modeled ET disturbance. Therefore, a limitation of these methods is that the changes to water balance following fires should be considered more theoretical, given the general difficulty in evaluating all the relevant fluxes and states simulated by the LSM. As the focus of the present study is to demonstrate the impacts of LAI-DA and the soil hydrophobicity parameterization, we consider the calibration to be beyond the scope of this work. We also acknowledge that the absence of calibration and the biases observed during verification limit the use of these approaches for deterministic forecasting, unless additional development is undertaken. Though the consistency of the results of simulating the soil disturbance with the observed hydrologic response and the fire-hydrology literature is encouraging, inconsistencies against other data products of ET and runoff highlight the need for better evaluation and benchmarking of the post-fire hydrological responses. Studying the broader applicability for our hydrophobicity approach would also require additional case-studies in different environments, which is challenging given the paucity of stream gage data in regions affected by fires. However, our ensemble approach for hydrophobicity provides a generic approach for representing the uncertainty with soil impacts after a fire, model formulation biases notwithstanding.

The study provides insights on the relative roles of vegetation disturbance compared to soil disturbance after a fire for these specific cases. These modeled results show that the relative impact of vegetation losses, as realized through the DA-VEG simulation, is greater than the impacts of soil hydrophobicity, based on water balance changes. One possible reason for this is the dependency of the soil parameters on vegetation-focused quantities, as MTBS burn severity may correlate with the impacts of the LAI DA. We, again, emphasize that the MTBS dataset was chosen for this proof of concept due to its consistency across events and expected availability for any large fire event across the US. Other proxies, such as BAER data are not available for as many cases. For both the Big Sur and Bryson cases, the relative impacts of vegetation losses on the water balance are greater and persist for longer than for soil disturbance.

However, the soil disturbance still plays a significant role in the surface runoff component, particularly for the Big Sur case (increasing from 5.7% to 7.3% of the total water balance). Additionally, it is important to note that the impacts of hydrophobicity are important during high flow events for both cases. The ensemble spread of the DA-VEG-SOIL simulations shows some solutions with significantly higher flow; this approach accounts for the spatial uncertainty of post-fire soil disturbances and their potential implications for flooding.

This study models the impact of hydrophobicity through an ensemble setup, acknowledging the underlying uncertainties in the hydrophobicity parametrization. There is uncertainty in the volume of surface runoff changes over time, suggesting that some hydrophobicity combinations, as realized through our ensemble system, can result in more flooding than others. An example of the ensemble spread is seen with the Bryson case, with a smaller burn area relative to the drainage basin. These variations likely also reflect uncertainties in hydrologic connectivity, where some ensemble members permit more hillslope runoff to reach channels. For the case studies considered here, the impacts of soil hydrophobicity are smaller on average; however, some ensemble simulations show more significant changes to surface runoff, thus suggesting that even small burn areas could yield more significant hydrologic changes after fires. Additional testing in other domains would be required to determine if these findings are also applicable elsewhere. The ensemble spread from the Bryson case, likely also reflects the more severe burn area (despite the relatively small area) for this case, as our parameterization increases runoff parameters more for more severe burns (based on the MTBS dataset).

There is some uncertainty in the relative roles of the wetter than average year following the fires and the hydrologic impacts of the fires (e.g., Wagenbrenner et al. 2021) for these cases. WY2017 was wetter than average for much of California, and this was the year immediately following the wildfires. While the Big Sur case was associated with a greater modeled hydrologic response, much of the burn area was less severe (Figure 3). Thus, our LAI assimilation and soil hydrophobicity parameterization remain fairly sensitive to lower severity wildfires. Note that the diminished impact of hydrophobicity in this basin in later years was likely also due to the modeled recovery of soils, where heavy precipitation results in soil parameters returning to normal more quickly. The Bryson, CA case was associated with higher burn severity in some areas; however, these effects are somewhat masked by the lower burn area relative to the size of the basin. This is likely why the hydrologic impacts of the wildfire for the Bryson, CA case shown here are less compared to the control simulation.

Another area of uncertainty in the wildfire parameterization presented here is the constraint of soil hydrophobicity based on burn severity. These limitations were described in detail in section 2.3. Technically, a hydrophobicity constraint based on soil burn severity (e.g., calibrated dNBR measurements) could add value to our parameterization, as Moody et al. (2016) show the direct linear relationship between dNBR and soil characteristics. However, the benefit of the approach outlined here is its utility for use with fire cases without additional site-specific field measurements. The MTBS dataset, due to its availability for all fires greater than 1,000 acres that occurred since 1984, allows us to parameterize fire impacts without additional datasets. Furthermore, the severity of hydrophobicity based on MTBS impacts has been demonstrated by Ebel et al. (2022), and the magnitude of soil hydrophobicity has also been parameterized based on vegetation disturbances, more broadly, by Thomas et al. (2021). The selection of the recovery timescale with a random distribution also ensures that the spatial uncertainty of the impacts of hydrophobicity are adequately accounted for (e.g., Wagenbrenner et al. 2021). The results in

Figures 11e and 12e demonstrate that there is considerable spread in the modeled surface runoff with the ensembles (as noted above), for both case studies.

In the present study, we demonstrate the relative roles of vegetation losses and soil hydrophobicity, with a remote-sensing observation-driven approach. We emphasize that these findings are for two specific cases that are relatively close to one another, in Central California. We used LAI DA combined with a novel hydrophobicity parameterization that accounts for burn severity and potential uncertainty in soil changes through an ensemble approach. From this analysis, we find that soil hydrophobicity post-fire plays a smaller role in hydrologic response, but is still capable of significantly increasing runoff during heavy precipitation events, for these cases. Further investigation with a large sample of test basins in different environments is needed to establish the generalizability of these findings. The framework presented in this paper enables a baseline for implementing and evaluating additional enhancements, including the use of a calibrated model or alternate burn severity datasets (e.g., BAER). Ground reference datasets around fire events are also needed to refine the parameterizations related to the modeling of post-fire soil repellency.

Acknowledgements

This research was supported by funding from NASA Headquarters for the Earth Information System (EIS) pilot study. Computing was supported by the resources at the NASA Center for Climate Simulation (NCCS) at NASA Goddard Space Flight Center.

Open Data Statement

The NASA LIS Model is available online at: https://github.com/NASA-LIS/LISF. The MERRA and IMERG atmospheric forcing and precipitation datasets are located online at https://disc.gsfc.nasa.gov/datasets?project=MERRA-2 and https://gpm.nasa.gov/data/directory respectively. USGS streamflow data are stored at: https://waterservices.usgs.gov/. The MODIS LAI product is available at: https://lpdaac.usgs.gov/products/mcd15a2hv006/, and the MODIS fire product is available at: https://lpdaac.usgs.gov/products/mcd64a1v006/. MTBS burn data may be downloaded from the following link: https://www.mtbs.gov/direct-download.

References

Abatzoglou, J. T., Rupp, D. E., O'Neill, L. W., & Sadegh, M. (2021). Compound Extremes Drive the Western Oregon Wildfires of September 2020. *Geophysical Research Letters*, *48*(8). https://doi.org/10.1029/2021GL092520

Abolafia-Rosenzweig, R., He, C., Chen, F., Zhang, Y., Dugger, A., Livneh, B., & Gochis, D. (2024). Evaluating Noah-MP simulated runoff and snowpack in heavily burned Pacific-Northwest snow dominated catchments. *Journal of Geophysical Research: Atmospheres*, 129, e2023JD039780. https://doi.org/10.1029/2023JD039780

Albergel, C., Munier, S., Bocher, A., Bonan, B., Zheng, Y., Draper, C., Leroux, D., & Calvet, J.-C. (2018). LDAS-Monde Sequential Assimilation of Satellite Derived Observations Applied to the Contiguous US: An ERA-5 Driven Reanalysis of the Land Surface Variables. *Remote Sensing*, *10*(10), 1627. https://doi.org/10.3390/rs10101627

Anderegg, W.R., Schwalm, C., Biondi, F., Camarero, J.J., Koch, G., Litvak, M., Ogle, K., Shaw, J.D., Shevliakova, E., Williams, A.P. and Wolf, A., (2015). Pervasive drought legacies in forest ecosystems and their implications for carbon cycle models. *Science*, *349* (6247), 528-532., doi: 10.1126/science.aab1833.

Anderson, M.C., Gao, F., Knipper, K., Hain, C., Dulaney, W., Baldocchi, D.D., Eichelmann, E., Hemes, K.S., Yang, Y., Medellín-Azuara, J., and Kustas, W.P., (2018) Field-scale assessment of land and water use change over the California Delta using remote sensing. *Remote Sens.* 10 889, https://doi.org/10.3390/rs10060889.

Ball, J. T., Woodrow, I. E., & Berry, J. A. (1987). A model predicting stomatal conductance and its contribution to the control of photosynthesis under different environmental conditions. In J. Biggins (Ed.), *Process in Photosynthesis Research* (Vol. 1, pp. 221–234). Martinus Nijhoff. Available online at: https://link.springer.com/chapter/10.1007/978-94-017-0519-6_48

Barlage, M., F. Chen, R. Rasmussen, Z. Zhang, and G. Miguez-Macho, (2021), The Importance of Scale-Dependent Groundwater Processes in Land-Atmosphere Interactions Over the Central United States. *Geophys Res Lett*, **48**, https://doi.org/10.1029/2020GL092171.

Bart, R. R. (2016). A regional estimate of postfire streamflow change in California. *Water Resources Research*, *52*(2), 1465–1478. https://doi.org/10.1002/2014WR016553

Blount, K., Ruybal, C. J., Franz, K. J., & Hogue, T. S. (2020). Increased water yield and altered water partitioning follow wildfire in a forested catchment in the western United States. *Ecohydrology*, *13*(1). https://doi.org/10.1002/eco.2170

Heavy Precipitation Events California and Northern Nevada January and February 2017. (2017). CNRFC. Available Online At: www.cnrfc.noaa.gov/storm_summaries/janfeb2017storms.php

Cai, X., Yang, Z.-L., David, C. H., Niu, G.-Y., and Rodell, M. (2014), Hydrological evaluation of the Noah-MP land surface model for the Mississippi River Basin, *J. Geophys. Res. Atmos.*, 119, 23–38, https://doi.org/10.1002/2013JD020792.

Cai, X., Yang, Z.-L., Xia, Y., Huang, M., Wei, H., Leung, L. R., and Ek, M. B. (2014), Assessment of simulated water balance from Noah, Noah-MP, CLM, and VIC over CONUS using the NLDAS test bed, *J. Geophys. Res. Atmos.*, 119, 13,751–13,770, https://doi.org/10.1002/2014JD022113.

Chen, L., Li, Y., Chen, F., Barr, A., Barlage, M., and Wan, B., (2016). The incorporation of an organic soil layer in the Noah-MP land surface model and its evaluation over a boreal aspen forest, *Atmos. Chem. Phys.,* 16, 8375–8387, https://doi.org/10.5194/acp-16-8375-2016

DeBano, L. F. (2000). The role of fire and soil heating on water repellency in wildland environments: a review. *Journal of Hydrology*, *231–232*, 195–206. https://doi.org/10.1016/S0022-1694(00)00194-3

Dickinson, R. E., Shaikh, M., Bryant, R., & Graumlich, L. (1998). Interactive Canopies for a Climate Model. *Journal of Climate*, *11*(11), 2823–2836. https://doi.org/10.1175/1520-0442(1998)011<2823:ICFACM>2.0.CO;2

Dominguez, F., H. Hu, and J. A. Martinez, (2020), Two-Layer Dynamic Recycling Model (2L-DRM): Learning from Moisture Tracking Models of Different Complexity. *J Hydrometeorol*, **21**, 3–16, https://doi.org/10.1175/JHM-D-19-0101.1.

Ebel, B.A., Rengers, F.K., Tucker, G.E., (2016). Observed and simulated hydrologic response for a first-order catchment during extreme rainfall 3 years after wildfire disturbance. *Water Resour. Res.* 52 (12), 9367–9389. https://doi.org/10.1002/2016WR019110.

Ebel, B. A., Romero, O. C., & Martin, D. A. (2018). Thresholds and relations for soil-hydraulic and soil-physical properties as a function of burn severity 4 years after the 2011 Las Conchas Fire, New Mexico, USA. *Hydrological Processes*, *32*(14), 2263–2278. https://doi.org/10.1002/hyp.13167

Ebel, B. A. (2020). Temporal evolution of measured and simulated infiltration following wildfire in the Colorado Front Range, USA: Shifting thresholds of runoff generation and hydrologic hazards. *Journal of Hydrology*, *585*, 124765. https://doi.org/10.1016/j.jhydrol.2020.124765

Ebel, B.A., Moody, J.A., Martin, D.A., (2022). Post-fire temporal trends in soil-physical and-hydraulic properties and simulated runoff generation: insights from different burn severities in the 2013 Black Forest Fire, CO, USA. *Sci. Total Environ.* 802, 149847 https://doi.org/10.1016/j.scitotenv.2021.149847.

Eidenshink, J., Schwind, B., Brewer, K., Zhu, Z.-L., Quayle, B., & Howard, S. (2007). A Project for Monitoring Trends in Burn Severity. *Fire Ecology*, *3*(1), 3–21. https://doi.org/10.4996/fireecology.0301003

Erlingis, J., M. Rodell, C.D. Peters-Lidard, B. Li, S.V. Kumar, J.S. Famiglietti, S.L. Granger, J.V. Hurley, P.-W. Liu, and D. Mocko, (2021). A High-Resolution Land Data Assimilation System Optimized for the Western United States, Journal of the American Water Resources Association, 1-19, https://doi.org/10.1111/1752-1688.12910.

Farres, P. J. (1987). The dynamics of rainsplash erosion and the role of soil aggregate stability. *CATENA*, *14*(1–3), 119–130. https://doi.org/10.1016/S0341-8162(87)80009-7

Fernández-Raga, M., Palencia, C., Keesstra, S., Jordán, A., Fraile, R., Angulo-Martínez, M., & Cerdà, A. (2017). Splash erosion: A review with unanswered questions. *Earth-Science Reviews*, *171*, 463–477. https://doi.org/10.1016/j.earscirev.2017.06.009

Flannigan, M., Cantin, A. S., de Groot, W. J., Wotton, M., Newbery, A., & Gowman, L. M. (2013). Global wildland fire season severity in the 21st century. *Forest Ecology and Management*, *294*, 54–61. https://doi.org/10.1016/j.foreco.2012.10.022

Gao, Y., Xiao, L., Chen, D., and coauthors (2017). Quantification of the relative role of land-surface processes and large-scale forcing in dynamic downscaling over the Tibetan Plateau. Clim Dyn 48, 1705–1721, https://doi.org/10.1007/s00382-016-3168-6

Gelaro, R., McCarty, W., Suárez, M. J., Todling, R., Molod, A., Takacs, L., Randles, C. A., Darmenov, A., Bosilovich, M. G., Reichle, R., Wargan, K., Coy, L., Cullather, R., Draper, C., Akella, S., Buchard, V., Conaty, A., da Silva, A. M., Gu, W., … Zhao, B. (2017). The Modern-Era Retrospective Analysis for Research and Applications, Version 2 (MERRA-2). *Journal of Climate*, *30*(14), 5419–5454. https://doi.org/10.1175/JCLI-D-16-0758.1

Getirana, A., A. Boone, D. Yamazaki, B. Decharme, F. Papa, N. Mognard, (2012). The hydrological modeling and analysis platform (HyMAP): Evaluation in the Amazon basin. *J. Hydrometeorol.***13**, 1641–1665, https://doi.org/10.1175/JHM-D-12-021.1.

Getirana, A., Kumar, S., Girotto, M., Rodell, M., (2017a). Rivers and floodplains as key components of global terrestrial water storage variability. Geophysical Research Letters, 44. https://doi.org/10.1002/2017GL074684

Getirana, A., Peters-Lidard, C., Rodell, M., Bates, P.D., (2017b). Trade-off between cost and accuracy in large-scale surface water dynamic modeling. Water Resources Research. https://doi.org/10.1002/2017WR020519

Getirana, A., Kumar, S., Konapala, G., Ndehedehe, C.E., (2021). Impacts of fully coupling land surface and flood models on the simulation of large wetlands' water dynamics: the case of the Inner Niger Delta. J. Adv. Model. Earth Syst. https://doi.org/10.1029/2021MS002463

Gibbons, J. D., and Chakraborti., S., (2011). *Nonparametric Statistical Inference*, 5th Ed., Boca Raton, FL: Chapman & Hall/CRC Press, Taylor & Francis Group.

Giglio, L., Justice, C., Boschetti, L., & Roy, D. (2015). *MCD64A1 MODIS/Terra+Aqua Burned Area Monthly L3 Global 500m SIN Grid V006 [Data set]*. NASA EOSDIS Land Processes Distributed Active Archive Center.

Cuevas-González, M., Gerard, F., Balzter, H. And Riaño, D. (2009), Analysing forest recovery after wildfire disturbance in boreal Siberia using remotely sensed vegetation indices. *Global Change Biology,* 15: 561-577. https://doi.org/10.1111/j.1365-2486.2008.01784.x

Hallema, D. W., Sun, G., Bladon, K. W., Norman, S. P, Caldwell, P. V., Liu, Y., & McNulty, S. G. (2017), Regional patters of postwildfire streamflow response in the Western United States: The importance of scale-specific connectivity. *Hydrological Processes*, *31*(14), 2582–2598. https://doi.org/10.1002/hyp.11208

Higuera, P. E., & Abatzoglou, J. T. (2021). Record-setting climate enabled the extraordinary 2020 fire season in the western United States. *Global Change Biology*, *27*(1), 1–2. https://doi.org/10.1111/gcb.15388

Higuera, P. E., Shuman, B. N., & Wolf, K. D. (2021). Rocky Mountain subalpine forests now burning more than any time in recent millennia. *Proceedings of the National Academy of Sciences*, *118*(25). https://doi.org/10.1073/pnas.2103135118

Hubbert, K. R., Wohlgemuth, P. M., Beyers, J. L., Narog, M. G., & Gerrard, R. (2012). Post-Fire Soil Water Repellency, Hydrologic Response, and Sediment Yield Compared between Grass-Converted and Chaparral Watersheds. *Fire Ecology*, *8*(2), 143–162. https://doi.org/10.4996/fireecology.0802143

Huffman, G.J., Bolvin, D.T., Braithwaite, D., Hsu, K., Joyce, R., Xie, P. and Yoo, S.H., (2015). NASA global precipitation measurement (GPM) integrated multi-satellite retrievals for GPM (IMERG). *Algorithm Theoretical Basis Document (ATBD) Version*, *4*, p.26.

Hoch, O. J., McGuire, L. A., Youberg, A. M., & Rengers, F. K. (2021). Hydrogeomorphic Recovery and Temporal Changes in Rainfall Thresholds for Debris Flows Following Wildfire. *Journal of Geophysical Research: Earth Surface*, *126*(12). https://doi.org/10.1029/2021JF006374

Hu, J. M., & Nolin, A. W. (2020). Widespread warming trends in storm temperatures and snowpack fate across the Western United States. *Environmental Research Letters*, *15*(3), 034059. https://doi.org/10.1088/1748-9326/ab763f

Kumar, S., Peters-Lidard, C., Tian, Y., Houser, P., Geiger, J., Olden, S., Lighty, L., Eastman, J., Doty, B., & Dirmeyer, P. (2006). Land information system: An interoperable framework for high resolution land surface modeling. *Environmental Modelling & Software*, *21*(10), 1402–1415. https://doi.org/10.1016/j.envsoft.2005.07.004

Kumar, S. v., Reichle, R. H., Koster, R. D., Crow, W. T., & Peters-Lidard, C. D. (2009). Role of subsurface physics in the assimilation of surface soil moisture observations. *Journal of Hydrometeorology*, *10*(6), 1534–1547. https://doi.org/10.1175/2009JHM1134.1

Kumar, S. V., Holmes, T., Andela, N., Dharssi, I., Vinodkumar, Hain, C., Peters-Lidard, C., Mahanama, S. P., Arsenault, K. R., Nie, W., & Getirana, A. (2021). The 2019–2020 Australian Drought and Bushfires Altered the Partitioning of Hydrological Fluxes. *Geophysical Research Letters*, *48*(1). https://doi.org/10.1029/2020GL091411

Kumar, S. v., Jasinski, M., Mocko, D. M., Rodell, M., Borak, J., Li, B., Beaudoing, H. K., & Peters-Lidard, C. D. (2019). NCA-LDAS Land Analysis: Development and Performance of a Multisensor, Multivariate Land Data Assimilation System for the National Climate Assessment. *Journal of Hydrometeorology*, *20*(8), 1571–1593. https://doi.org/10.1175/JHM-D-17-0125.1

Kumar, S., Getirana, A., Libonati, R., Hain, C., Mahanama, S., & Andela, N. (2022). Changes in land use enhance the sensitivity of tropical ecosystems to fire-climate extremes. *Scientific Reports*, *12*(1), 964. https://doi.org/10.1038/s41598-022-05130-0

Lahmers, T. M., S. V. Kumar, D. Rosen, A. Dugger, D. J. Gochis, J. A. Santanello, C. Gangodagamage, and R. Dunlap, (2022), Assimilation of NASA's Airborne Snow Observatory snow measurements for improved hydrological modeling: A case study enabled by the coupled LIS/WRF-Hydro system. *Water Resour Res*, 58(3), https://doi.org/10.1029/2021WR029867.

Li, F., Lawrence, D. M., & Bond-Lamberty, B. (2017). Impact of fire on global land surface air temperature and energy budget for the 20th century due to changes within ecosystems. *Environmental Research Letters*, *12*(4), 044014. https://doi.org/10.1088/1748-9326/aa6685

Lin, P., L. J. Hopper, Z. Yang, M. Lenz, and J. W. Zeitler, (2018), Insights into Hydrometeorological Factors Constraining Flood Prediction Skill during the May and October 2015 Texas Hill Country Flood Events. *J. Hydrometeor.*, **19**, 1339–1361, https://doi.org/10.1175/JHM-D-18-0038.1.

Ma, N., Niu, G.-Y., Xia, Y., Cai, X., Zhang, Y., Ma, Y., & Fang, Y. (2017). A systematic evaluation of Noah-MP in simulating land-atmosphere energy, water, and carbon exchanges over the continental United States. *Journal of Geophysical Research: Atmospheres*, 122, 12,245–12,268. https://doi.org/10.1002/2017JD027597

Ma, Q., Bales, R. C., Rungee, J., Conklin, M. H., Collins, B. M., & Goulden, M. L. (2020). Wildfire controls on evapotranspiration in California's Sierra Nevada. *Journal of Hydrology*, *590*, 125364. https://doi.org/10.1016/j.jhydrol.2020.125364

McGuire, L. A., Rengers, F. K., Youberg, A. M., Gorr, A. N., Hoch, O. J., Beers, R., and Porter, R. (2023) Characteristics of debris flow prone watersheds and triggering rainstorms following the Tadpole Fire, New Mexico, USA, EGUsphere [preprint], https://doi.org/10.5194/egusphere-2023-1672.

McKee, T. B., Doesken, N. J., & Kleist, J. (1993). The relationship of drought frequency and duration to time scales. *Proceedings of the 8th Conference on Applied Climatology*. Available online at: https://www.droughtmanagement.info/literature/AMS_Relationship_Drought_Frequency_Duration_Time_Scales_1993.pdf

McNally, A., Jacob, J., Arsenault, K., Slinski, K., Sarmiento, D. P., Hoell, A., Pervez, S., Rowland, J., Budde, M., Kumar, S., Peters-Lidard, C., and Verdin, J. P. (2022). A Central Asia hydrologic monitoring dataset for food and water security applications in Afghanistan, Earth Syst. Sci. Data, 14, 3115–3135, https://doi.org/10.5194/essd-14-3115-2022

Melton, F.S., Huntington, J., Grimm, R., Herring, J., Hall, M., Rollison, D., Erickson, T., Allen, R., Anderson, M., Fisher, J.B., Kilic, A., Senay, G.B., Volk, J., Hain, C., Johnson, L., Ruhoff, A., Blankenau, P., Bromley, M., Carrara, W., Daudert, B., Doherty, C., Dunkerly, C., Friedrichs, M., Guzman, A., Halverson, G., Hansen, J., Harding, J., Kang, Y., Ketchum, D., Minor, B., Morton, C., Ortega-Salazar, S., Ott, T., Ozdogan, M., ReVelle, P.M., Schull, M., Wang, C., Yang, Y., & Anderson, R.G. (2021), OpenET: Filling a Critical Data Gap in Water Management for the Western United States. *Journal of the American Water Resources Association.* 58 971-994, https://doi.org/10.1111/1752-1688.12956.

Mocko, D. M., Kumar, S. v., Peters-Lidard, C. D., & Wang, S. (2021). Assimilation of Vegetation Conditions Improves the Representation of Drought over Agricultural Areas. *Journal of Hydrometeorology*, *22*(5), 1085–1098. https://doi.org/10.1175/JHM-D-20-0065.1

Moritz, M. A., Parisien, M.-A., Batllori, E., Krawchuk, M. A., van Dorn, J., Ganz, D. J., & Hayhoe, K. (2012). Climate change and disruptions to global fire activity. *Ecosphere*, *3*(6), art49. https://doi.org/10.1890/ES11-00345.1

Moody, J. A., Shakesby, R. A., Robichaud, P. R., Cannon, S. H., & Martin, D. A. (2013). Current research issues related to post-wildfire runoff and erosion processes. *Earth-Science Reviews*, *122*, 10–37. https://doi.org/10.1016/j.earscirev.2013.03.004

Moody, J. A., Ebel, B. A., Nyman, P., Martin, D. A., Stoof, C., & McKinley, R. (2016). Relations between soil hydraulic properties and burn severity. *International Journal of Wildland Fire*, *25*(3), 279. https://doi.org/10.1071/WF14062

Niu, G.-Y., Yang, Z.-L., Dickinson, R. E., Gulden, L. E., & Su, H. (2007). Development of a simple groundwater model for use in climate models and evaluation with Gravity Recovery and Climate Experiment data. *Journal of Geophysical Research*, *112*(D7), D07103. https://doi.org/10.1029/2006JD007522

Niu, G.-Y., Yang, Z.-L., Mitchell, K. E., Chen, F., Ek, M. B., Barlage, M., Kumar, A., Manning, K., Niyogi, D., Rosero, E., Tewari, M., & Xia, Y. (2011). The community Noah land surface model with multiparameterization options (Noah-MP): 1. Model description and evaluation with local-scale measurements. *Journal of Geophysical Research*, *116*(D12), D12109. https://doi.org/10.1029/2010JD015139

Nie, W., Kumar, S. v., Peters-Lidard, C. D., Zaitchik, B. F., Arsenault, K. R., Bindlish, R., & Liu, P. (2022). Assimilation of Remotely Sensed Leaf Area Index Enhances the Estimation of Anthropogenic Irrigation Water Use. *Journal of Advances in Modeling Earth Systems*, *14*(11). https://doi.org/10.1029/2022MS003040

Parsons, A., Robichaud, P. R., Lewis, S. A., Napper, C., & Clark, J. T. (2010). Field guide for mapping post-fire soil burn severity. Fort Collins, CO: U.S. Department of Agriculture, Forest Service, Rocky Mountain Research Station. https://doi.org/10.2737/RMRS-GTR-243

Perkins, J. P., Diaz, C., Corbett, S. C., Cerovski-Darriau, C., Stock, J. D., Prancevic, J. P., Micheli, E., & Jasperse, J. (2022). Multi-Stage Soil-Hydraulic Recovery and Limited Ravel

Accumulations Following the 2017 Nuns and Tubbs Wildfires in Northern California. *Journal of Geophysical Research: Earth Surface*, *127*(6). https://doi.org/10.1029/2022JF006591

Peters-Lidard, C. D., Kumar, S. v., Mocko, D. M., & Tian, Y. (2011). Estimating evapotranspiration with land data assimilation systems. *Hydrological Processes*, *25*(26), 3979–3992. https://doi.org/10.1002/hyp.8387

Pilotto, I.L., Rodríguez, D.A., Tomasella, J. and coauthors, (2015). Comparisons of the Noah-MP land surface model simulations with measurements of forest and crop sites in Amazonia. *Meteorol Atmos Phys* **127**, 711–723. https://doi.org/10.1007/s00703-015-0399-8

Prats, S. A., Wagenbrenner, J. W., Martins, M. A. S., Malvar, M. C., & Keizer, J. J. (2016). Mid-term and scaling effects of forest residue mulching on post-fire runoff and soil erosion. *Science of The Total Environment*, *573*, 1242–1254. https://doi.org/10.1016/j.scitotenv.2016.04.064

Rasmussen, R. M., and Coauthors, 2023: CONUS404: The NCAR–USGS 4-km Long-Term Regional Hydroclimate Reanalysis over the CONUS. *Bull. Amer. Meteor. Soc.*, **104**, E1382–E1408, https://doi.org/10.1175/BAMS-D-21-0326.1.

Reichle, R. H., McLaughlin, D. B., & Entekhabi, D. (2002). Hydrologic data assimilation with the ensemble Kalman filter. *Monthly Weather Review*, *130*(1), 103–114. https://doi.org/10.1175/1520-0493(2002)130<0103:HDAWTE>2.0.CO;2

Reilly, M. J., Dunn, C. J., Meigs, G. W., Spies, T. A., Kennedy, R. E., Bailey, J. D., & Briggs, K. (2017). Contemporary patterns of fire extent and severity in forests of the Pacific Northwest, USA (1985-2010). *Ecosphere*, *8*(3), e01695. https://doi.org/10.1002/ecs2.1695

Robichaud, P. R., Wagenbrenner, J. W., Pierson, F. B., Spaeth, K. E., Ashmun, L. E., & Moffet, C. A. (2016). Infiltration and interrill erosion rates after a wildfire in western Montana, USA. *CATENA*, *142*, 77–88. https://doi.org/10.1016/j.catena.2016.01.027

Sabater, J. M., Rüdiger, C., Calvet, J.-C., Fritz, N., Jarlan, L., & Kerr, Y. (2008). Joint assimilation of surface soil moisture and LAI observations into a land surface model. *Agricultural and Forest Meteorology*, *148*(8–9), 1362–1373. https://doi.org/10.1016/j.agrformet.2008.04.003

Saxe, S., Hogue, T. S., & Hay, L. (2018). Characterization and evaluation of controls on post-fire streamflow response across western US watersheds. *Hydrology and Earth System Sciences*, *22*(2), 1221–1237. https://doi.org/10.5194/hess-22-1221-2018

Thomas, M. A., Rengers, F. K., Kean, J. W., McGuire, L. A., Staley, D. M., Barnhart, K. R., & Ebel, B. A. (2021). Postwildfire Soil-Hydraulic Recovery and the Persistence of Debris Flow Hazards. *Journal of Geophysical Research: Earth Surface*, *126*(6). https://doi.org/10.1029/2021JF006091

Tijdeman, E., Stahl, K., & Tallaksen, L. M. (2020). Drought Characteristics Derived Based on the Standardized Streamflow Index: A Large Sample Comparison for Parametric and Nonparametric Methods. *Water Resources Research*, *56*(10). https://doi.org/10.1029/2019WR026315

Vieira, D. C. S., Malvar, M. C., Fernández, C., Serpa, D., & Keizer, J. J. (2016). Annual runoff and erosion in a recently burn Mediterranean forest – The effects of plowing and time-since-fire. *Geomorphology*, *270*, 172–183. https://doi.org/10.1016/j.geomorph.2016.06.042

Wagenbrenner, J. W., Ebel, B. A., Bladon, K. D., & Kinoshita, A. M. (2021). Post-wildfire hydrologic recovery in Mediterranean climates: A systematic review and case study to identify current knowledge and opportunities. *Journal of Hydrology*, *602*, 126772. https://doi.org/10.1016/j.jhydrol.2021.126772

Wang, Z., Bovik, A. C., Sheikh, H. R. & Simoncelli, E. P. (2004). Image Quality Assessment From Error Visibility to Structural Similarity. *IEEE Transactions on Image Processing* **13**, 600–612.

Wilcoxon signed rank test. (2024). MathWorks. Available Online At: https://www.mathworks.com/help/stats/signrank.html#References

Williams, A. P., Abatzoglou, J. T., Gershunov, A., Guzman-Morales, J., Bishop, D. A., Balch, J. K., & Lettenmaier, D. P. (2019). Observed Impacts of Anthropogenic Climate Change on Wildfire in California. *Earth's Future*, *7*(8), 892–910. https://doi.org/10.1029/2019EF001210

Williams, A. P., and co-authors, (2022). Growing impact of wildfire on western US water supply. *Proc. Natl. Acad. Sci.* 119, e2114069119. https://doi.org/10.1109/TIP.2003.819861.

Yamazaki, D., D. Ikeshima, J. Sosa, P. D. Bates, G. H. Allen, T. M. Pavelsky, (2019). MERIT Hydro: A High-Resolution Global Hydrography Map Based on Latest Topography Dataset. *Water Resour. Res.*, https://doi.org/10.1029/2019WR024873

Table 1: Parameters for meteorological forcing and model state variables for EnKF MODIS LAI DA configuration.

Variable	**Perturbation Type**	**Std. Dev.**	**Cross Correlation across variables**		
Meteorological Forcing			**SW correlation**	**LW correlation**	**PCP correlation**
Downward Shortwave (SW)	Multiplicative	0.3	1.0	-0.5	-0.8
Downward Longwave (LW)	Additive	30	-0.5	1.0	0.5
Precipitation (PCP)	Multiplicative	0.5	-0.8	0.5	1.0
Noah-MP LSM LAI states			**LAI**		
Leaf Area Index (LAI)	Additive	0.01	1.0		

Table 2: Percent of evapotranspiration (ET), runoff, and TWS changes (and sub-components) of total precipitation for the OL, DA-VEG, and DA-VEG-SOIL simulations for USGS gage 11143000 for one year after the fire. The ET (transpiration, canopy evaporation, and soil evaporation), runoff (surface and sub-surface), and TWS changes (0-2.0 m soil moisture and ground water) are shown as percentages of the total precipitation, starting on the fire ignition date (22 July 2016).

Balance Component	**OL**	**DA-VEG**	**DA-VEG-SOIL**
Transpiration	24.7	16.9	16.8
Canopy Evaporation	5.4	3.4	3.4
Soil Evaporation	30.5	34.8	34.3
Total ET	**60.6**	**55.1**	**54.5**
Surface Runoff	5.0	5.7	7.3
Sub-Surface Runoff	23.4	26.2	25.3
Total Runoff	**28.4**	**31.9**	**32.6**
Soil Moisture Change	3.5	5.7	5.6
Groundwater Change	7.6	7.5	7.5
Total TWS Change	**11.1**	**13.2**	**13.1**

Table 3: Percent of evapotranspiration (ET), runoff, and TWS changes (and sub-components) of total precipitation for the OL, DA-VEG, and DA-VEG-SOIL simulations for USGS gage 11148900 for one year after the fire. The ET (transpiration, canopy evaporation, and soil evaporation), runoff (surface and sub-surface), and TWS changes (0-2.0 m soil moisture and ground water) are shown as percentages of the total precipitation, starting on the fire ignition date (13 August 2016).

Balance Component	**OL**	**DA-VEG**	**DA-VEG-SOIL**
Transpiration	23.4	21.6	21.4
Canopy Evaporation	3.3	3.0	3.0
Soil Evaporation	33.0	34.1	34.2
Total ET	**59.7**	**58.7**	**58.6**
Surface Runoff	4.8	5.3	5.4
Sub-Surface Runoff	22.4	24.4	24.5
Total Runoff	**27.2**	**29.7**	**29.9**
Soil Moisture	3.7	3.0	3.0
Groundwater	9.5	8.7	8.6
Total TWS	**13.2**	**11.7**	**11.6**

Table 4: Percent differences of transpiration, bare soil evaporation, canopy evaporation, surface runoff and sub-surface runoff for the DA-VEG and DA-VEG-SOIL simulations compared to the OL simulation for the area upstream of USGS Gages 11143000 and 11148900.

Simulation Difference (%-Change)	Transpiration	Soil Evaporation	Canopy Evaporation	**Total ET**	Surface Runoff	Sub-surface Runoff	**Total Runoff**
	USGS 11143000						
DA-VEG (year-1)	-31.70*	14.01*	-36.66*	-9.09*	13.66*	11.93*	12.23*
DA-VEG -SOIL (year-1)	-32.16*	12.47*	-37.04*	-10.09*	46.09*	8.00*	14.68*
DA-VEG (year-2)	-16.59*	14.13*	-16.14*	-3.39*	3.11*	5.31*	4.94*
DA-VEG -SOIL (year-2)	-16.89*	14.06*	-16.48*	-3.60*	6.17*	4.90*	5.12*
DA-VEG (year-3)	-12.20*	10.41*	-20.42*	-2.28*	17.45*	34.56*	30.52*
DA-VEG -SOIL (year-3)	-12.48*	10.45*	-20.79*	-2.42*	18.69*	35.22*	31.31*
	USGS 11148900						
DA-VEG (year-1)	-7.62*	3.36*	-9.84*	-1.67*	9.95*	8.59*	8.83*
DA-VEG -SOIL (year-1)	-8.64*	3.61*	-10.73*	-1.98*	12.35*	9.28*	9.82*
DA-VEG (year-2)	-6.21*	5.63*	-14.18*	-1.24*	1.52*	2.14*	2.02*
DA-VEG -SOIL (year-2)	-6.80*	6.02*	-14.85*	-1.40*	2.83*	2.35*	2.44*
DA-VEG (year-3)	-2.78*	2.70*	-5.84*	-0.09	5.44*	9.51*	8.62*
DA-VEG -SOIL (year-3)	-3.73*	2.93*	-6.58*	-0.39	9.93*	10.57*	10.43*

**Indicates statistical significance compared from the Wilcoxon Signed Rank Test, compared to the OL simulation.*

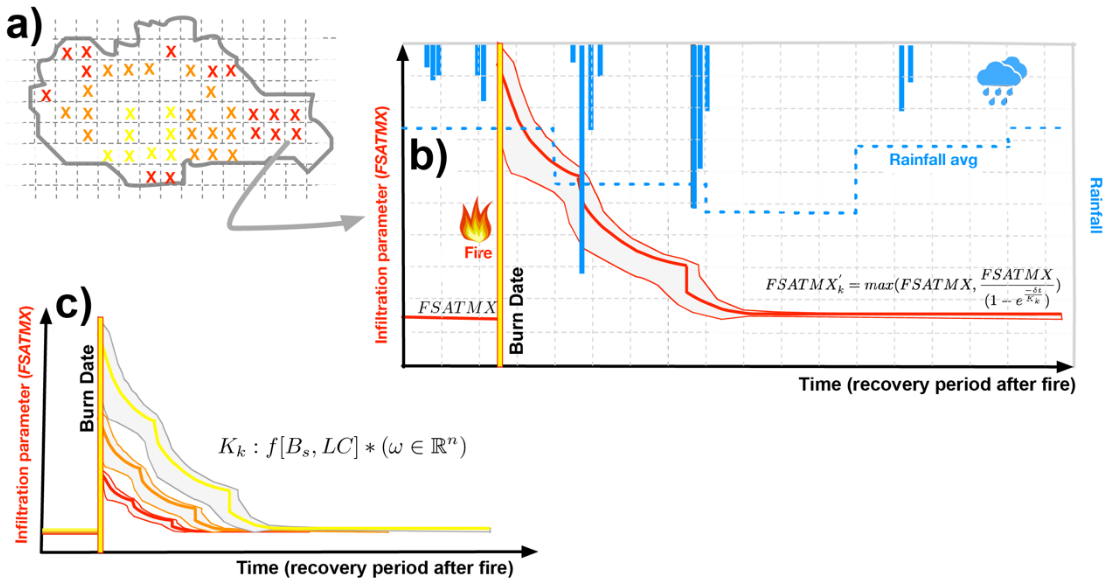

Figure 1: Schematic of the ensemble soil hydrophobicity parameterization with Noah-MP LSM. Panel (a) represents a fire polygon with crosses representing locations with different fire severity. Panel (b) shows the time evolution of FSATMX parameter following a fire event. The red line represents the ensemble mean and the shaded area represents the range of FSATMX for different ensemble members. The blue bars represent rainfall events whereas the dashed blue line represents the climatological rainfall average values. Panel (c) highlights the different levels of recovery simulated by the K_k parameter (3 levels are shown), which is defined as a function of Burned severity (B_s), Landcover type (LC), and recovery time scale factor (ω), which lengthens or shortens the recovery time scale for FSATMX. Three example burn severity levels are shown in panel c, including low (red), moderate (orange), and high (yellow).

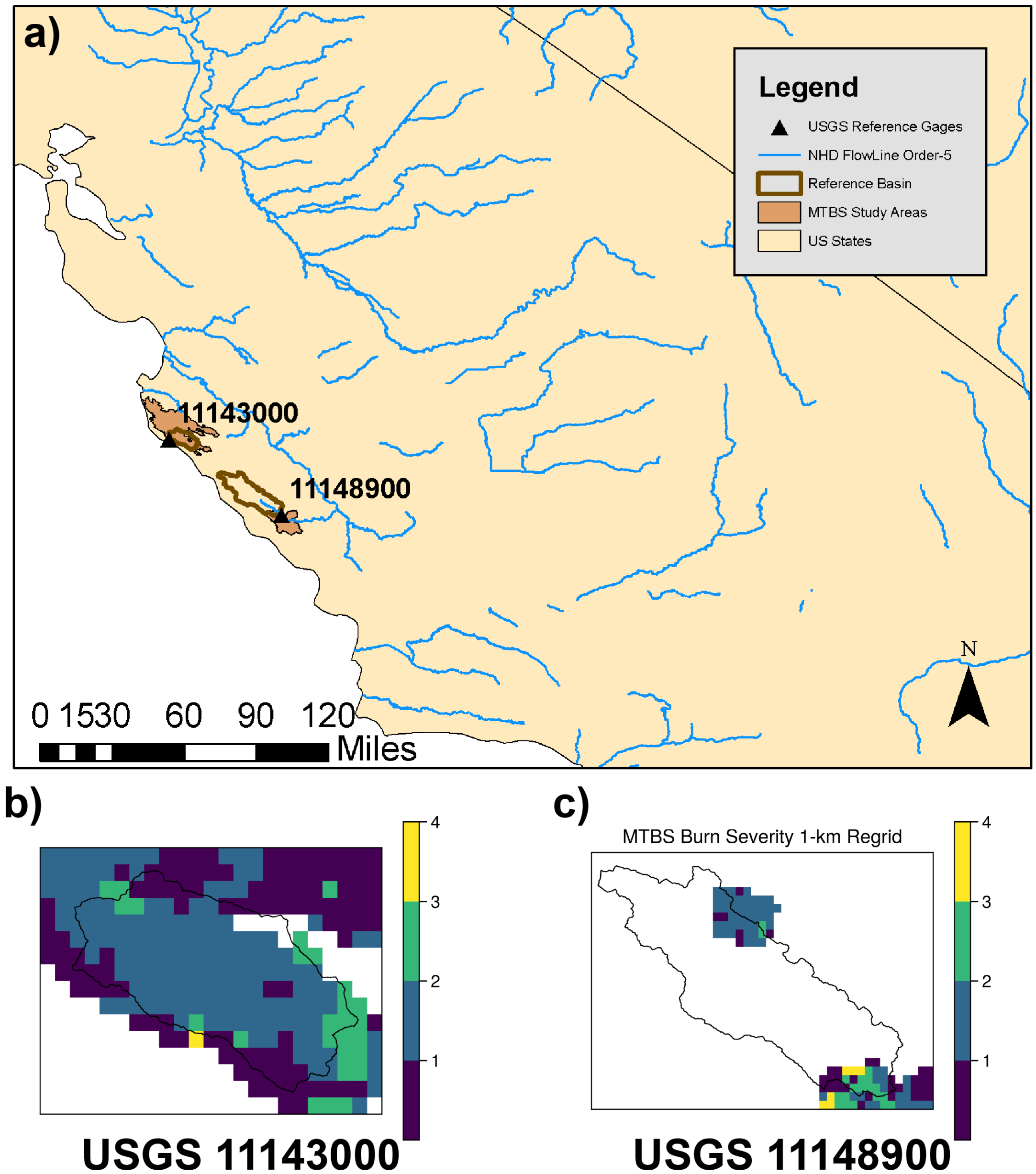

Figure 2: The two fire burn areas and corresponding USGS gages, relative to Northern California, are shown (panel a). The regridded Monitoring Trends in Burn Severity (MTBS) burn categories for the 0.01 degree model domains (used for simulations), next to analysis USGS basins, are plotted for USGS gage 11143000 (panel b) and USGS gage 11148900 (panel c). For regridded burn severity maps, uncolored areas are not covered in the MTBS area (assumed to be unburned). Colored MTBS categories represent: 1) unburned/unchanged, 2) low severity, 3) moderate severity, and 4) high severity.

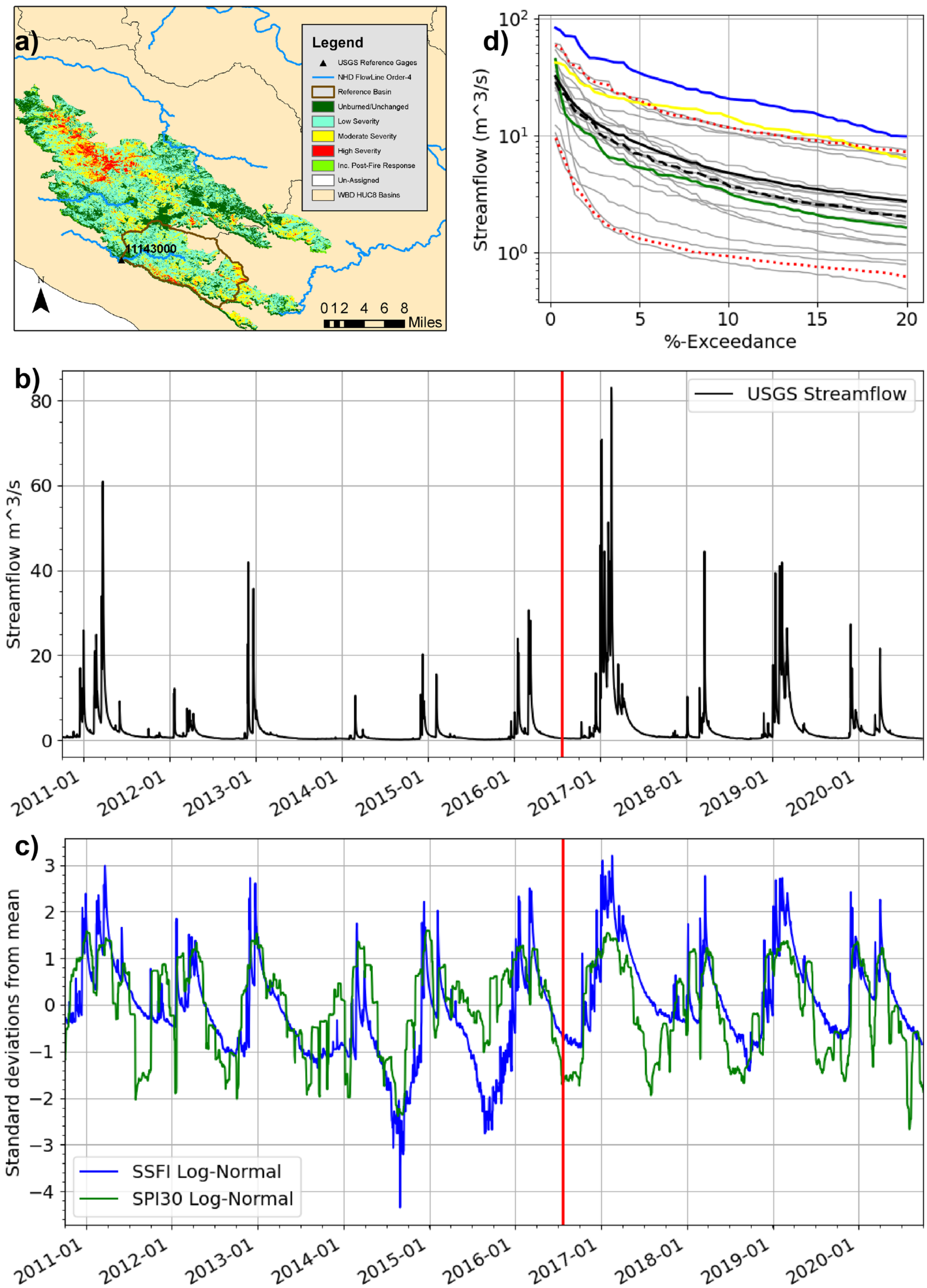

Figure 3: Fire Characteristics and impact on hydrologic response for the 2016 fire affecting Big Sur State Park. MTBS fire severity from the event is plotted with the USGS Watershed

Boundary Dataset (WBD) HUC8 basins, National Hydrography Dataset (NHD) order-3 and higher streams, and USGS gages-II reference gage 11143000. The reference basin for gage 11143000 is also plotted (a). Observed streamflow at USGS gage 11143000 (b), and 30-day mean standardized precipitation index (SPI) with standardized streamflow index (SSFI) based on a 3-parameter log-normal distribution for USGS gage 11143000 are plotted from WY2011 through WY2020 (c). The vertical red line in panels b and c is the date for the fire ignition. The annual flow duration curve for the top 20 percentile highest flows is plotted for WY2001 through WY2022 (d). This figure includes the mean flow duration curve (solid black line), median flow duration curve (dashed black line), 5th and 95th percentile flow duration curve (dashed red line), year-1 post-fire flow duration curve (WY 2017; solid blue line), year-2 post-fire flow duration curve (WY2018; solid green line), year-3 post-fire flow duration curve (WY2019; solid yellow line), and all other years (solid grey line). All FDC statistics exclude the three burn years.

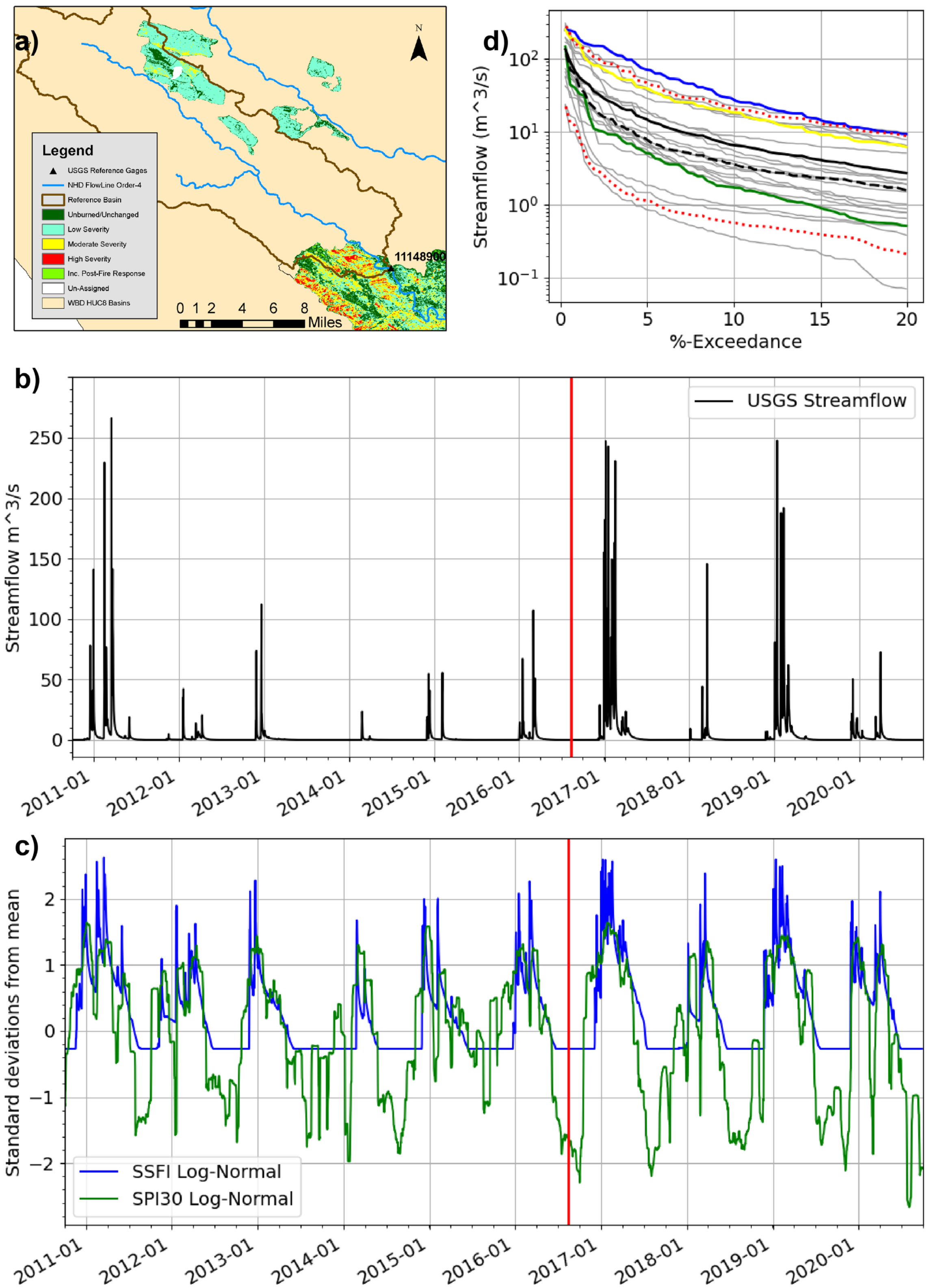

Figure 4: Fire Characteristics and impact on hydrologic response for the 2016 fire affecting Bryson, CA. MTBS fire severity from the event is plotted with the USGS WBD HUC8 basins,

NHD order-3 and higher streams, and USGS gages-II reference gage 11148900. The reference basin for gage 11148900 is also plotted (a). Observed streamflow at USGS gage 11148900 (b), and 30-day mean standardized precipitation index (SPI) with standardized streamflow index (SSFI) based on 3-parameter log-normal distribution for USGS gage 11148900 are plotted from WY2011 through WY2022 (c). The vertical red line in panels b and c is the date for the fire ignition. The annual flow duration curve for the top 20 percentile highest flows is plotted for WY2001 through WY2022 (d). This figure includes the mean flow duration curve (solid black line), median flow duration curve (dashed black line), 5th and 95th percentile flow duration curve (dashed red line), year-1 post-fire flow duration curve (WY 2017; solid blue line), year-2 post-fire flow duration curve (WY2018; solid green line), year-3 post-fire flow duration curve (WY2019; solid yellow line), and all other years (solid grey line). All FDC statistics exclude the three burn years.

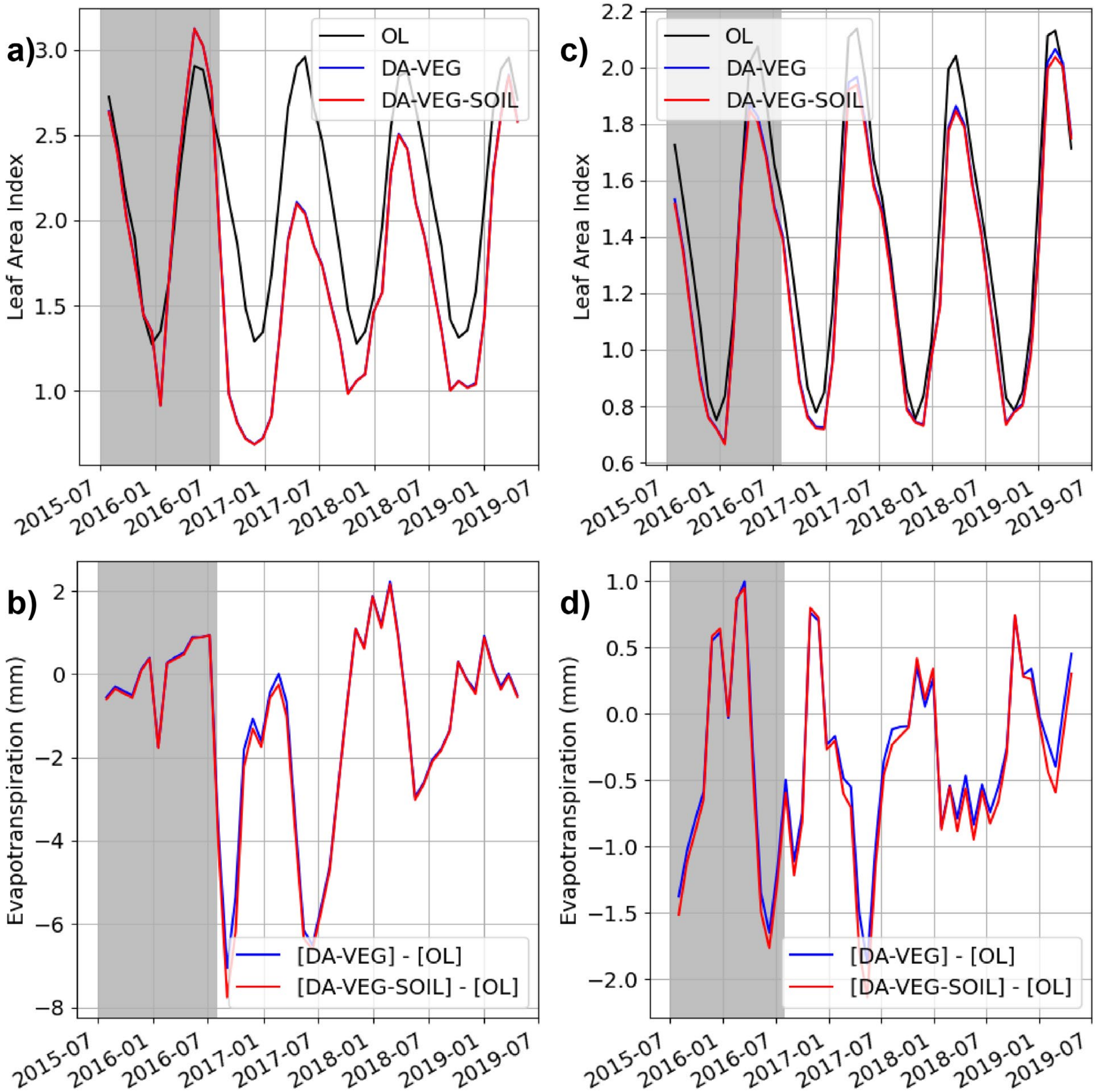

Figure 5: Monthly Leaf Area Index (a, c) for OL (black), DA-VEG (blue), and DA-VEG-SOIL (red) and differences in monthly ET (b, d) from the OL simulation for the DA-VEG (blue) and DA-VEG-SOIL (red) simulations for the basins upstream of each USGS gage site. Left panels (a, b) include data for USGS Gage 11143000, and right (c, d) panels include data for USGS Gage 11148900. The periods with gray shading indicate dates before the fire. Note that the DA-VEG and DA-VEG-SOIL lines overlap for most of the graphs, making them difficult to distinguish.

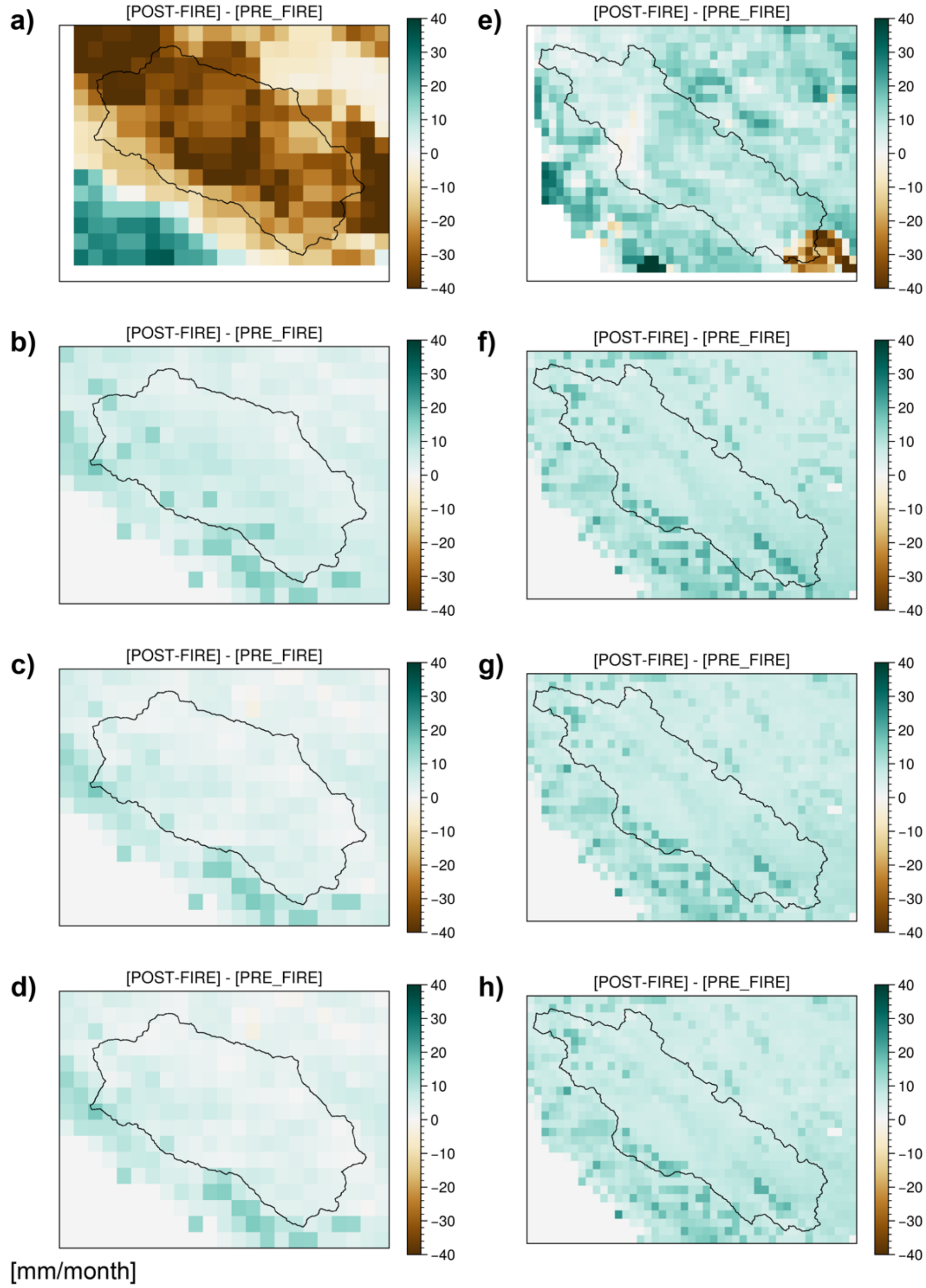

Figure 6: January through June change in ET (mm/month) for 2017 (post-fire) compared to 2016 (pre-fire). The USGS gage 11143000 basin (Big Sur case) is shown on the left and the USGS 11148900 basin (Bryson case) is shown on the right. From top to bottom, DisALEXI data (a,e), OL model output (b,f), DA-VEG model output (c,g), and DA-VEG-SOIL (d,h) model output are shown. Basin domains are also plotted with the gridded data.

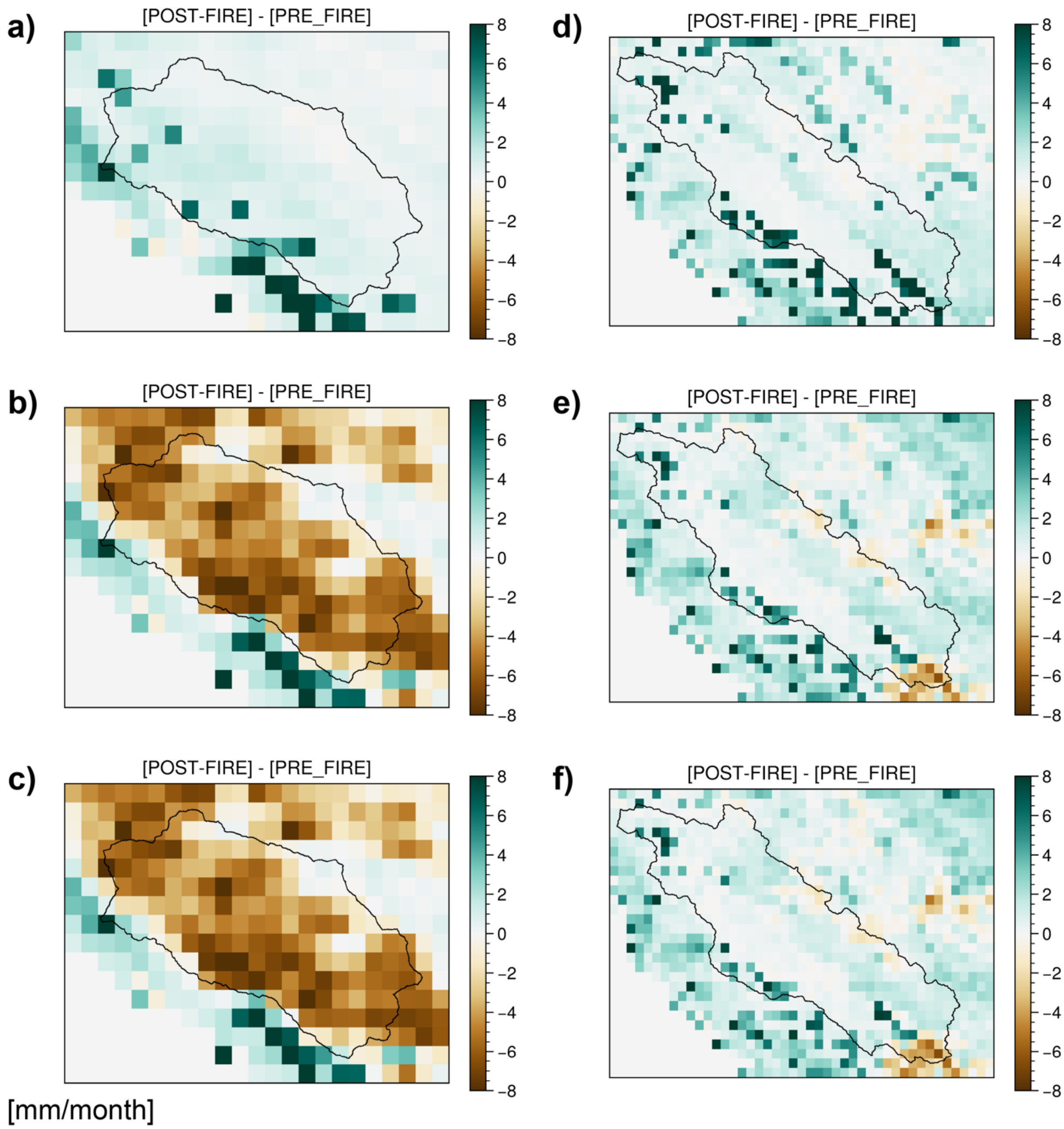

Figure 7: January through June change in Transpiration (mm/month) for 2017 (post-fire) compared to 2016 (pre-fire). The USGS gage 11143000 basin (Big Sur case) is shown on the left, and the USGS 11148900 basin (Bryson case) is shown on the right. From top to bottom, OL model output (a,d), and DA-VEG model output (b,e) and DA-VEG-SOIL (c,f) model output are shown. Basin domains are also plotted with the gridded data.

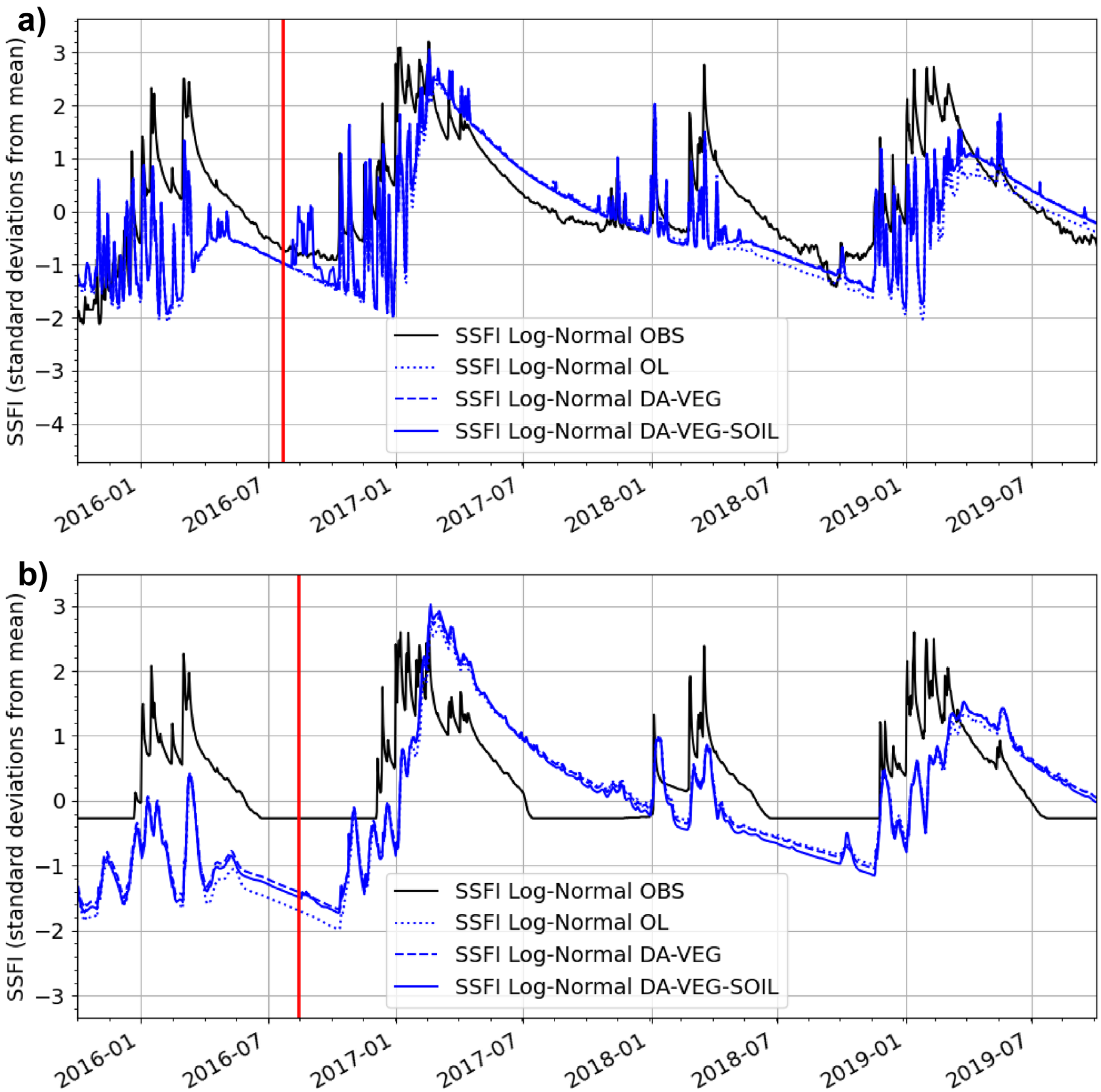

Figure 8: Standardized streamflow index (SSFI) based on a 3-parameter log-normal distribution for USGS gage 11143000 (a) and USGS gage 11148900 (b). Observations and OL, DA-VEG, and DA-VEG-SOIL simulations are shown.

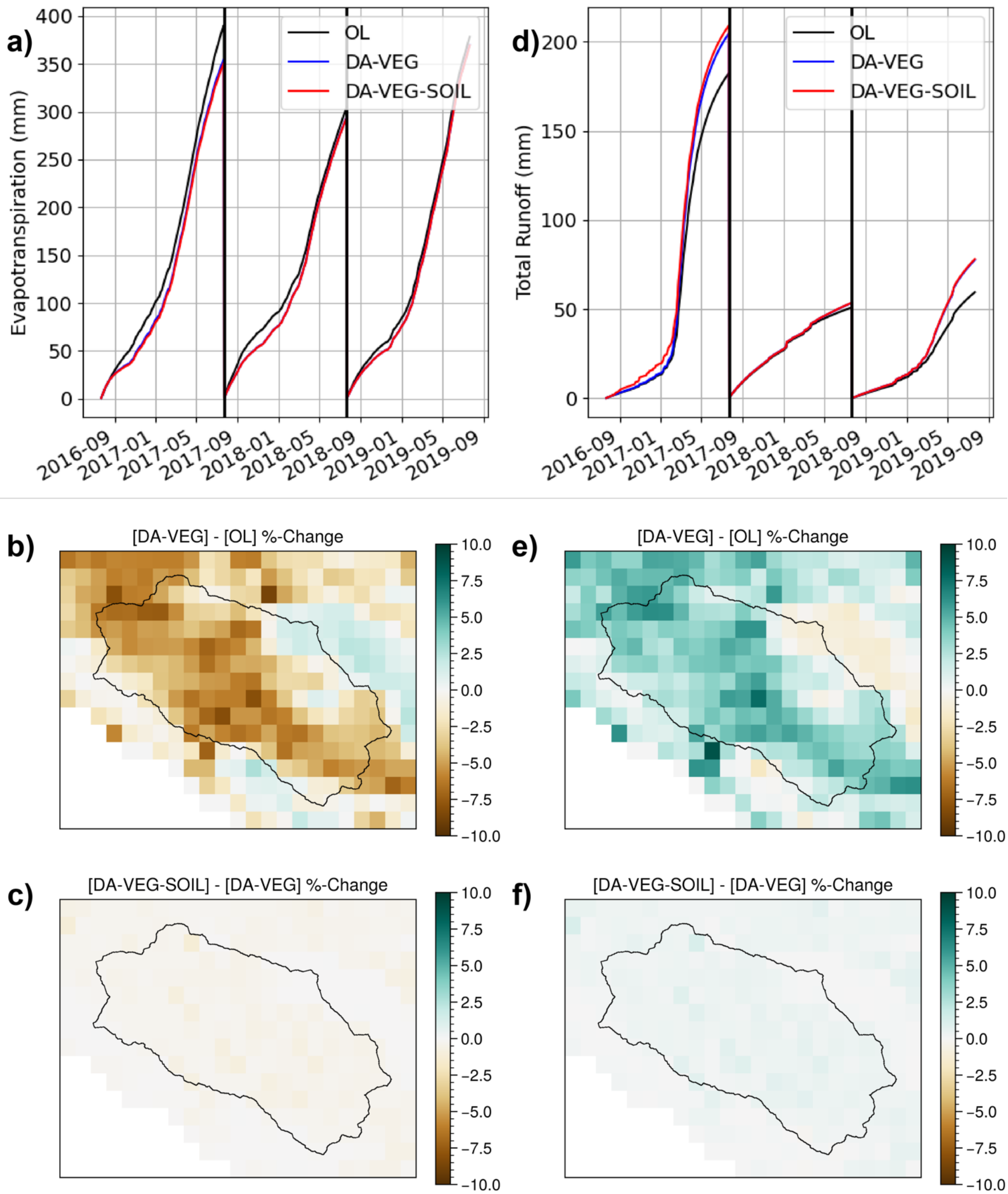

1334

1335 **Figure 9:** Accumulated ET (a) and total runoff (d) for the OL (black), DA-VEG (blue), and DA-
1336 VEG-SOIL (red) LSM simulations. Spatial changes to total (ET) (b, c) and total runoff (e, f) as a
1337 percentage of total precipitation for the DA-VEG vs OL simulations (middle) and DA-VEG-
1338 SOIL vs DA-VEG (bottom) simulations are shown. Fluxes are computed for the model domain
1339 of USGS gage 11143000, for three years after the fire (22 July 2016 to 22 July 2019).

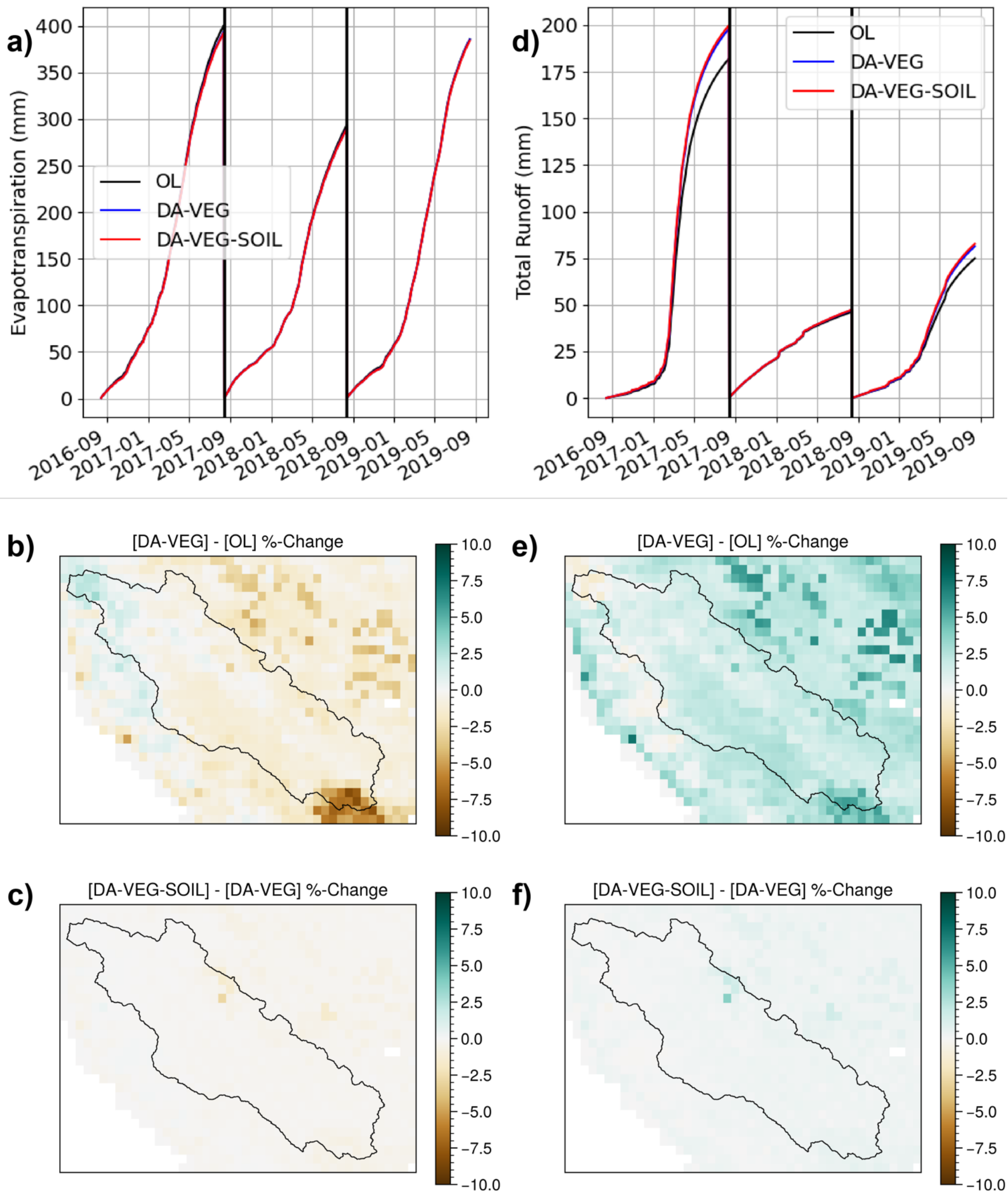

Figure 10: Accumulated ET (a) and total runoff (d) for the OL (black), DA-VEG (blue), and DA-VEG-SOIL (red) LSM simulations. Spatial changes to total (ET) (b, c) and total runoff (e, f) as a percentage of total precipitation for the DA-VEG vs OL simulations (middle) and DA-VEG-SOIL vs DA-VEG (bottom) simulations are shown. Fluxes are computed for the model domain of USGS gage 11148900 for three years after the fire (13 August 2016 to 13 August 2019).

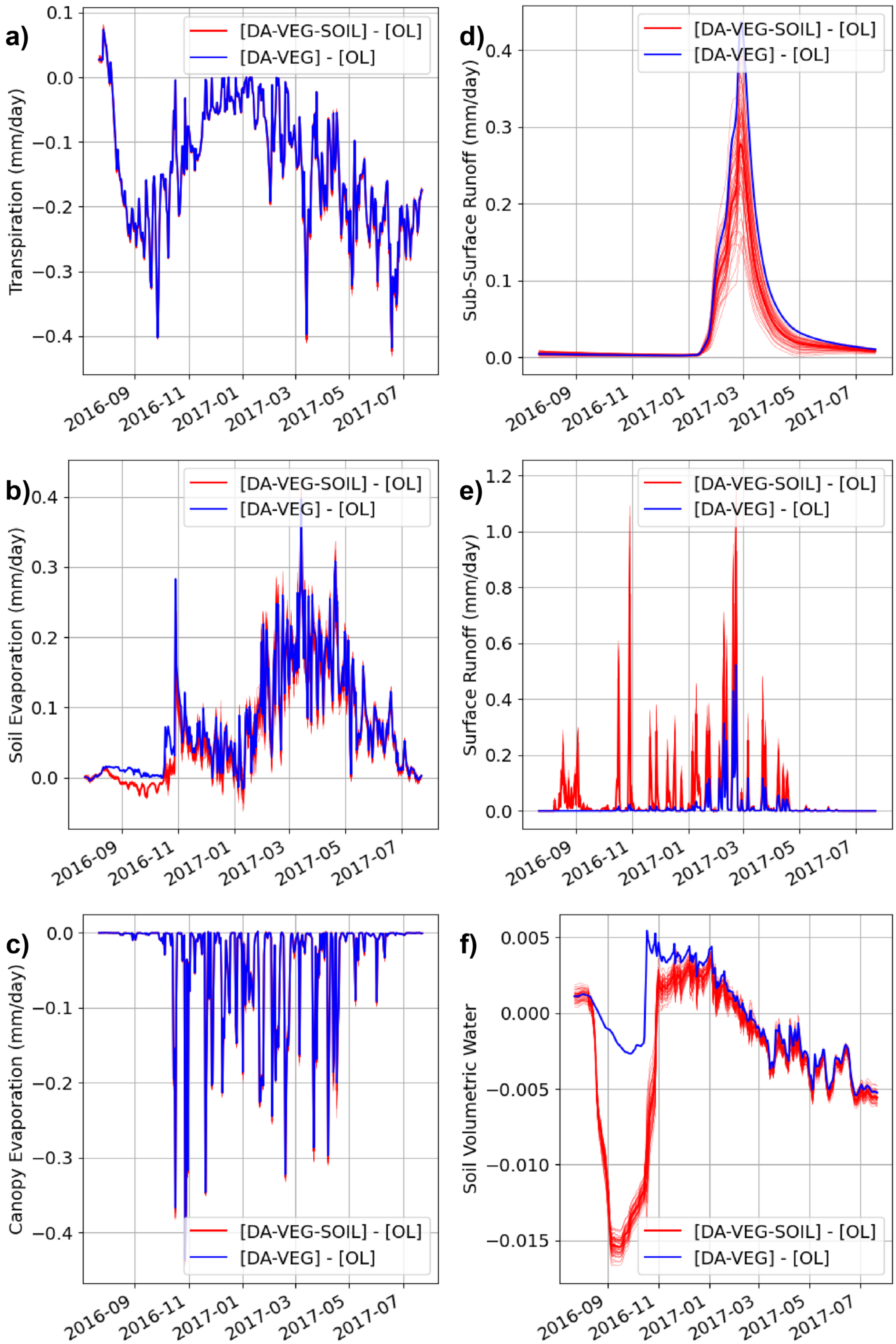
a)
b)
c)
d)
e)
f)
[DA-VEG-SOIL] - [OL]
[DA-VEG] - [OL]
Transpiration (mm/day)
Soil Evaporation (mm/day)
Canopy Evaporation (mm/day)
Sub-Surface Runoff (mm/day)
Surface Runoff (mm/day)
Soil Volumetric Water
2016-09
2016-11
2017-01
2017-03
2017-05
2017-07

1346

Figure 11: Differences in transpiration (a; top left), bare soil evaporation (b; middle left), canopy evaporation (c; bottom left), sub-surface runoff (d; top right), surface runoff (e; middle right) and 0-10 cm soil moisture (f; bottom right) from OL simulation for the DA-VEG (blue) and DA-VEG-SOIL (red) LSM simulations. Narrow red lines are for individual ensemble members of the DA-VEG-SOIL simulation, and the thick red line is for the ensemble mean. Fluxes are computed for the basin upstream of USGS gage 11143000 for up to one year after the fire (22 July 2016 to 22 July 2017).

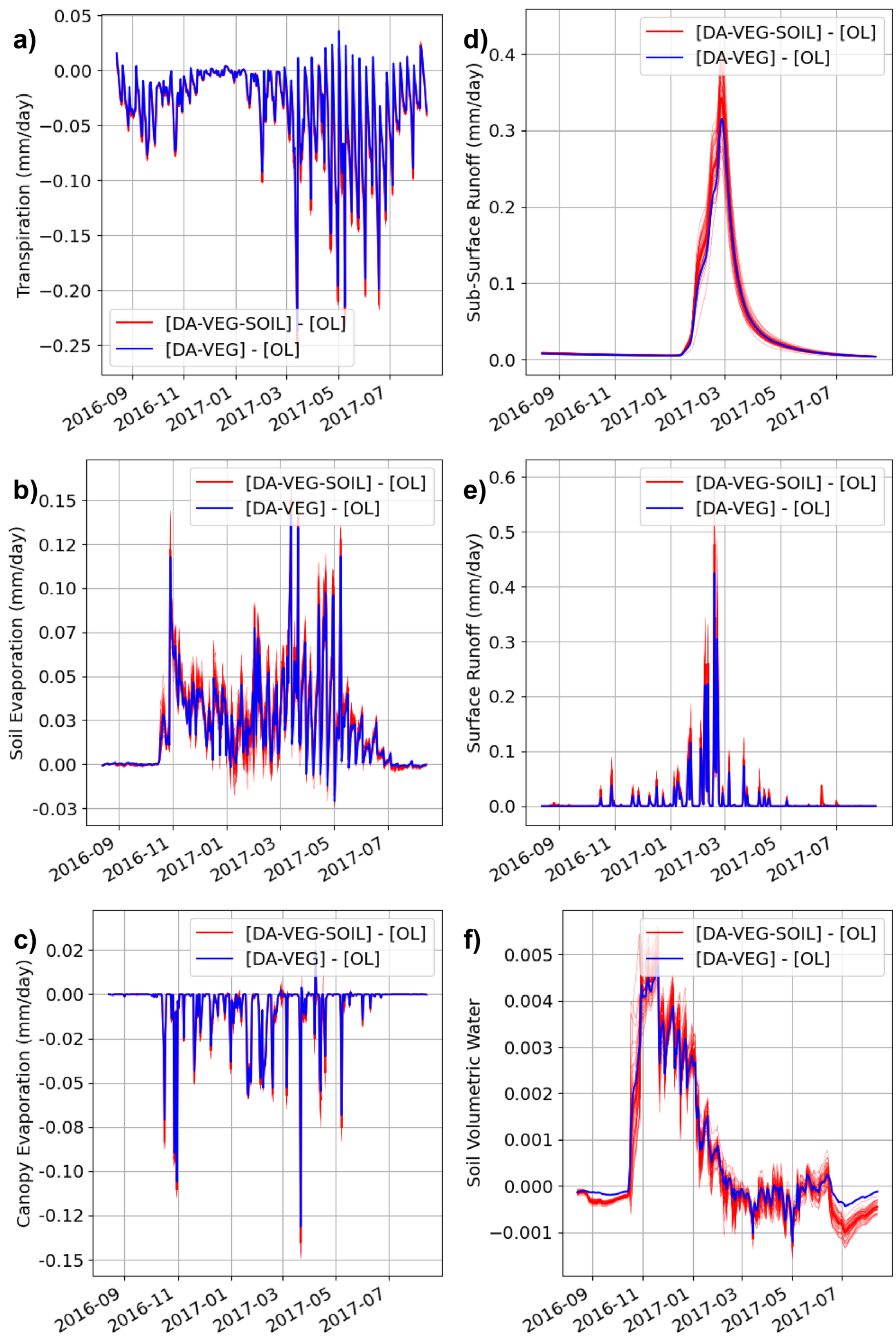
a)
Transpiration (mm/day)
[DA-VEG-SOIL] - [OL]
[DA-VEG] - [OL]
d)
Sub-Surface Runoff (mm/day)
b)
Soil Evaporation (mm/day)
e)
Surface Runoff (mm/day)
c)
Canopy Evaporation (mm/day)
f)
Soil Volumetric Water
2016-09
2016-11
2017-01
2017-03
2017-05
2017-07

1355

Figure 12: Differences in transpiration (a; top left), bare soil evaporation (b; middle left), canopy evaporation (c; bottom left), sub-surface runoff (d; top right), surface runoff (e; middle right) and 0-10 cm soil moisture (f; bottom right) from OL simulation for the DA-VEG (blue) and DA-VEG-SOIL (red) LSM simulations. Narrow red lines are for individual ensemble members DA-VEG-SOIL simulation, and the thick red line is for the ensemble mean. Fluxes are computed for the basin upstream of USGS gage 11148900 for up to one year after the fire (13 August 2016 to 13 August 2017).